

Shape matters: Lagrangian tracking of complex nonspherical microparticles in superellipsoidal approximation

Jana Wedel^{a,*}, Paul Steinmann^{a,b}, Mitja Štrakl^c, Matjaž Hriberšek^c, Jure Ravnik^c

^a Institute of Applied Mechanics, Universität Erlangen-Nürnberg, Germany

^b Glasgow Computational Engineering Center, University of Glasgow, United Kingdom

^c Faculty of Mechanical Engineering, University of Maribor, Slovenia

ARTICLE INFO

Keywords:

Non-spherical particles
Superellipsoids
CFD
OpenFOAM

ABSTRACT

Humans are constantly exposed to airborne pollutants such as pollen, exhaust residues, microplastics, fabrics, aerosols, or, as recently, ash particles from volcanic eruptions, which are rarely perfectly spherical. In order to reduce the impact of harmful particles or, on the contrary, to improve the targeted delivery of drugs, understanding the motion of complex shaped particles in fluid flows is of key interest. Common models mainly use shape factors to account for deviations from spherical shape, but these often fail to accurately predict particle motion. We advocate a more accurate modeling of complex particles by a superellipsoidal shape approximation, which allows covering a wide range of particle geometries. Superellipsoidal particle shapes allow for a novel approximation of translational and rotational resistance tensors, derived based on data from dedicated DNS computations. Our surrogate approach for convex bodies ($\epsilon_1, \epsilon_2 \in (0, 2)$), implemented in OpenFOAM[®] based on Lagrangian particle tracking, is first validated based on experimental and in-silico results from the literature, followed by a comparison of the effects of non-sphericity for some well known fluid flow cases, such as a lid-driven cavity (validated for $Re = 470$, $St = 0.0023$), pipe flow (validated for $Re = 137$, $St = 0.01$) and a simplified bifurcation (validated for $Re = 500$, $St = 0.5 \times 10^{-2} - 0.5$). We show that using shape factor assisted spherical or ellipsoidal approximations of the particles leads to insufficient accuracy of computation of the particle's trajectory, whereas the newly derived superellipsoidal drag and torque models proved to provide a superior accuracy of the Lagrangian particle tracking over simplified non-spherical particle approximations.

1. Introduction

Most man-made and naturally occurring particles such as fibers, blood cells, pollen and microplastics are rarely perfectly spherical. As Feng and Kleinstreuer (2013) stated, fluid-particle dynamics are affected by the size, density, and shape of the particle under consideration, as well as the interaction between the particle and the surrounding geometry. Besides, the authors found that arbitrarily shaped particles exhibit complex dynamics due to shape anisotropy and therefore rotational motions must be considered, (Feng and Kleinstreuer, 2013). However, in various references, the particles are assumed to be spherical, (Koullapis et al., 2017, 2016). Exemplarily, this simplification holds for sufficiently small aerosols as they behave rigidly and form a spherical shape due to their high surface tension, (Balachandar et al., 2020; Wedel et al., 2021a,b, 2022). Nevertheless, there are several applications where this assumption no longer applies, such as the motion and deposition of fibers, (Dastan et al., 2014), or pollen particles, (Inthavong et al., 2021). In particular, elongated particles such as

asbestos fibers tend to align with the airflow, resulting in a significantly deviating trajectory compared to a sphere of the same volume, (Feng and Kleinstreuer, 2013). In this context, Su and Cheng (2006) conjectured that inhalation of elongated rather than spherical particles poses a higher risk to the respiratory tract as they can penetrate deeper into the airways, (Su and Cheng, 2006). These examples underline that the assumption of spherical particles is only justified in isolated applications.

The most commonly employed non-spherical particle shape is ellipsoidal, called prolate if its two smaller semi-axes are equal in size and oblate if its two major semi-axis are equal. In *in silico* studies, prolate and oblate ellipsoids are commonly considered due to the fact that they possess no geometric discontinuity and are therefore denoted as mathematically-treatable, (Saccone et al., 2022), see the excellent review of Voth and Soldati (2017). As stated by Voth and Soldati (2017), the point-particle approach is applicable if the particle

* Corresponding author.

E-mail address: jana.wedel@fau.de (J. Wedel).

size is smaller than the Kolmogorov length scale. Furthermore, the authors stated that particle inertia is usually negligible if the Stokes number is much smaller than one. It is also known that if the particle shape deviates from a perfect sphere, the interactions between fluid and particle are affected, since non-sphericity results in specific drag characteristics, (Voth and Soldati, 2017).

In general, ellipsoids are typically used to model fiber-like shapes, (Feng and Kleinstreuer, 2013; Belka et al., 2017). There are a number of experimental and numerical studies of the transport of ellipsoids for basic shear flows, i.e. Couette and Poiseuille flows. Jeffery (1922) investigated prolate ellipsoids in linear shear flows and found that the rotational period of the particles is related to the particle aspect ratio and the shear rate of the flow. In addition, Gallily and Eisner (1979) studied elongated particles in a 2D Poiseuille flow both theoretically and experimentally.

Zhang et al. (2001) were one of the first to numerically study ellipsoidal particles in turbulent channel flow while employing the point-particle approach. The authors studied the effect of particle aspect ratio and inertia on preferential concentration as well as wall accumulation. Furthermore, Tian et al. (2012) studied the motion of ellipsoidal particles and their deposition efficiency in a pipe flow. The authors found that the aspect ratio, the shear rate of the flow, and the ratio of particle to fluid density alter the particle motion, (Tian et al., 2012). In addition, Högberg et al. (2008) investigated the influence of Brownian motion on prolate ellipsoids of submicron size. Moreover, Feng and Kleinstreuer (2013) focused on the computational analysis of ellipsoids with varying aspect ratios and studied both stable and unstable rotational periods in tubular flows. Besides, several studies showed that fiber-like particles experience a preferential alignment with the mean flow direction within the near-wall region, however, in the core of the flow no such alignment is observed and the resulting orientations are more uniform, (Challabotla et al., 2016; Arcen et al., 2017). Furthermore, Cui et al. (2018a,b, 2019b) proposed a lift model to determine the lift forces acting on fibers, i.e. prolate ellipsoidal particles, in arbitrary nonuniform flows. In addition, Cui et al. (2019a) studied sludge flocs and proposed an advanced Lagrangian particle tracking approach that is able to account for non-spherical shapes, internal porosity and permeability as well as inhomogeneous mass distribution.

Recently, Zhang et al. (2020) performed particle-resolved bedload simulations for spherical and non-spherical particles in laminar and turbulent open channel flows. These authors showed that the onset of motion was directly influenced by the shape of the sediment particles. In addition, Jain et al. (2021) conducted simulations of bedload transport in open channels and studied particles of oblate, prolate, triaxial and spherical shapes. The authors found that the use of non-spherical shapes resulted in significant differences in particle motion compared to spherical shape, with prolate ellipsoids showing the strongest tendency to form clusters in the spanwise direction. Considering the results of Zhang et al. (2020) and Jain et al. (2021), Saccone et al. (2022) concluded that the tendency to orient in a preferred direction near a wall is a characteristic behavior of non-spherical particles. Furthermore, Michel and Arcen (2021) used direct numerical simulation (DNS) to study the dynamics of prolate ellipsoids in a turbulent channel flow. The authors investigated the effect of Reynolds number Re on the preferred particle orientation and concentration and found that as the friction Reynolds number Re_τ increases, the distribution approaches uniformity, with particle inertia having a notable and particle aspect ratio having a minor effect. In addition, Cui et al. (2021) studied the alignment of fiber- and disk-shaped particles in near-wall turbulence in a channel flow. The authors observed the presence of three preferred alignment patterns that the considered particles can form around ensemble-averaged vortices. More recently, Saccone et al. (2022) studied the effects of wall roughness on prolate particles in a turbulent channel flow. These authors showed that accounting for wall roughness resulted in a more homogeneous particle distribution in the direction

of the wall normal. In addition, the authors observed that particle elongation affected the preferred orientation, but less pronounced in the near-wall region than for smooth walls.

Besides, there are several experimental, (Belka et al., 2016; Myojo, 1987, 1990; Myojo and Takaya, 2001; Marijnissen et al., 1991; Su and Cheng, 2006; Okabe et al., 1997), and numerical studies, (Feng and Kleinstreuer, 2013; Belka et al., 2017), that have investigated the motion of ellipsoidal particles in complex geometries, such as human lung replicas. Recently, Lizal et al. (2022) experimentally studied the motion of glass fibers in a first airway bifurcation replica and provided important measurements to improve numerical simulations of fiber motion in human lungs. In fact, ellipsoidal particle models are often inadequate to reproduce realistic particle motion, see for example asbestos-like fibers as presented by Ravnik et al. (2022). The authors showed that the Stokes flow-induced drag and torque of asbestos-like fibers cannot be sufficiently reproduced by using an ellipsoidal shape approximation.

In general, for simplified particle shapes such as spheres or elongated ellipsoids the forces and torques can be determined analytically, (Jeffery, 1922; Brenner, 1964a). However, no such equations exist for arbitrarily shaped particles. Consequently, to account for non-spherical particles, various drag correlations have been proposed, (Hölzer and Sommerfeld, 2008; Wang et al., 2018; Bagheri and Bonadonna, 2016). Besides, lift and torque correlations have been introduced, however, solely for special shapes such as oblate ellipsoids or fibers, (Sanjeevi et al., 2018; Zastawny et al., 2012; Tian et al., 2012; Tian and Ahmadi, 2013). Nevertheless, in Štrakl et al. (2022a) we showed that these correlations are often insufficient to accurately reproduce the translational, rotational, and deformational particle resistance tensor. Moreover, we proposed a novel framework for predicting drag and torque of superellipsoidal particles by performing a large number of direct numerical simulations (DNS) of particles in Stokes flow. We showed that this framework enables accurate modeling for an unprecedented variety of particle shapes.

Although a few studies have been conducted for specific non-spherical particles such as rod-shaped or ellipsoidal fibers, (Cui et al., 2018a,b, 2019b; Fennelly, 2020; Belka et al., 2017), systematic research on a broad range of non-spherical particles is relatively sparse due to the experimental challenges in generating corresponding particles with a specific geometry, (Wu et al., 2021). In this context, superellipsoidal particles represent an opportunity to gain further insight into the motion and deposition of a wide variety of particle shapes and allows for an improved modeling of arbitrarily shaped particle dynamics.

This study focuses on the analysis of motion and deposition of particles with superellipsoidal shape. To this end, we present our novel superellipsoid particle tracking developed in OpenFoam[®] and based on Lagrangian particle tracking. The approach employs the superellipsoid surrogate approach proposed in our previous work, see Štrakl et al. (2022a,b). In the scope of this study, we compare the motion and deposition of different particle shapes, including spheres, ellipsoids and superellipsoids, fitted to a naturally occurring pollen particle. We obtained good agreement between the novel superellipsoid particle tracking solver and numerical and experimental studies that used spherical and ellipsoidal shapes. In general, we found a strong correlation between the shape of the particles and the resulting particle motion. Moreover, spherical (with and without shape factors) and prolate ellipsoidal shape approximations in particular were found to be insufficient to reproduce the trajectory and especially the rotational motion of a realistic particle such as the pollen replica considered. This is related to the resulting deviations in translation, rotation, and deformation tensor coefficients, which result in altered particle motion compared to the superellipsoidal reference shape. In case of the prolate ellipsoid, this lead to an extended time of passing through the flow-aligned orientation, i.e. where the particle long axis is aligned with the streamwise direction.

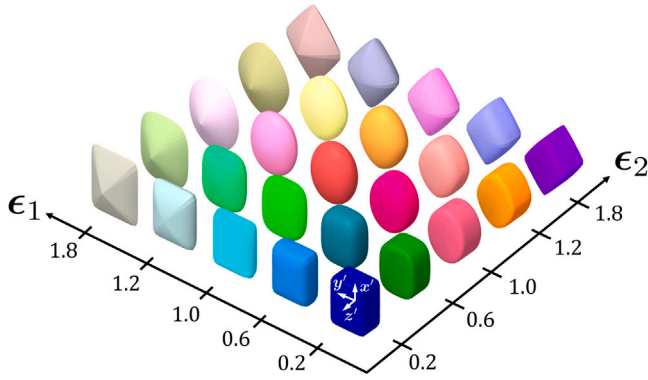


Fig. 1. Sketch of a representative set of superellipsoidal particles, with $\lambda_1 > \lambda_2$. Including schematic particle frame of reference (pFoR).

The paper is organized as follows: In Section 2, the novel superellipsoid particle force and torque model is introduced along with the novel deposition model. Moreover, in Section 3, the superellipsoid particle tracking is validated and applied to common cases, such as a lid-driven cavity flow and a simplified bifurcation. Finally, Section 4 summarizes the paper and presents the main conclusions.

For the notation of tensors and their corresponding coefficient matrices in various frames of references we refer to Cui et al. (2018a,b, 2019b).

2. Superellipsoids

2.1. General description of superellipsoid particles

Superellipsoidal particles, as introduced by Barr (1981), allow the modeling of particles with a more complex shape than spheres or ellipsoids. According to Barr (1981), superellipsoids can be described by the so-called inside-outside function:

$$S(r') = \left[\left[\frac{x'}{a} \right]^{2/\epsilon_2} + \left[\frac{y'}{b} \right]^{2/\epsilon_2} \right]^{\epsilon_2/\epsilon_1} + \left[\frac{z'}{c} \right]^{2/\epsilon_1}, \quad (1)$$

which is written in the particle frame of reference (pFoR). Any position $r' = [x', y', z']$ with $S(r') \leq 1$ belongs to the superellipsoid with $S(r') = 1$ describing the particle surface. The parameters a, b, c in Eq. (1) determine the dimensions of the superellipsoid, while the exponents ϵ_1 and ϵ_2 indicate the squareness of the shape in the x' or y' plane and z' direction, respectively. Note that $\epsilon_i \in (0, 2)$ represents a convex body bounded by a cuboid ($\epsilon_i \rightarrow 0$) and an octahedron ($\epsilon_i \rightarrow 2$), (Wellmann et al., 2008). Commonly, the superellipsoid particle is described by the aspect ratio, i.e. $\lambda_1 = a/c, \lambda_2 = b/c$. In the context of our model, we employ the following conventions: $a \geq b \geq c$ and followingly $\lambda_1 \geq \lambda_2 \geq 1$.

Furthermore, the volume of a superellipsoidal particle can be written as (Jaklič et al., 2000):

$$V = 2abc\epsilon_1\epsilon_2 B\left(\frac{\epsilon_1}{2} + 1, \epsilon_1\right) B\left(\frac{\epsilon_2}{2}, \frac{\epsilon_2}{2}\right), \quad (2)$$

where B is related to the Gamma function as follows (Jaklič et al., 2000):

$$B(x, y) = \frac{\Gamma(x)\Gamma(y)}{\Gamma(x+y)}. \quad (3)$$

Fig. 1 shows a set of representative convex superellipsoidal particles with $\lambda_1 > \lambda_2$ to illustrate the wide variety of geometries that can be obtained by applying the superellipsoid formulation. Note that the superellipsoid formulation includes prolate ellipsoids, see Fig. 1 $\epsilon_1 = \epsilon_2 = 1.0$, as well as spherical particles when $\lambda_1 = \lambda_2 = \epsilon_1 = \epsilon_2 = 1$.

2.2. Equation of motion for superellipsoidal particles

2.2.1. Dynamics of translational motion

In general, the trajectory of a particle is determined by its interaction with the surrounding fluid flow. For sufficiently small particles, e.g. in the micro- and submicron range, the particles can be described as rigid, i.e. their deformation is considered negligible. In this work, particle transport is described in an Euler-Lagrangian framework. Maxey and Riley (1983) proposed the equation of motion for small rigid particles. Furthermore, Brenner (1964b) presented the drag expression for arbitrary shaped particles. Followingly, we write (Maxey and Riley, 1983; Brenner, 1964b):

$$m_p \frac{d\mathbf{v}}{dt} = \mathbf{g}V_p [\rho_p - \rho_f] + V_p \rho_f \frac{D\mathbf{u}}{Dt} - \frac{1}{2} V_p \rho_f \left[\frac{d\mathbf{v}}{dt} - \frac{d\mathbf{u}}{dt} \right] + \pi \rho_f \nu_f c \mathbf{K} \cdot [\mathbf{u} - \mathbf{v}], \quad (4)$$

using the superellipsoidal surrogate approach as presented in Štrákl et al. (2022a). Eq. (4) considers gravity, buoyancy, pressure gradient, added mass and drag force, while neglecting the time history effects, aerodynamic lift as well as higher order terms, (Cui et al., 2018b). Here $\mathbf{v}, m_p, V_p, c, \rho_p$, denotes the particle velocity, mass, volume, smallest particle half axis and density, respectively. Note that $V_p = d_{eq}^3 \pi / 6$, see Eq. (2), is used to obtain the volume equivalent diameter of a sphere d_{eq} . Besides, $\mathbf{u}, \rho_f, \nu_f$ label the fluid velocity, fluid density and kinematic viscosity. In addition, \mathbf{K} is the translational resistance tensor. Note that in Eq. (4), $D/Dt = \partial/\partial t + [\mathbf{u} \cdot \nabla]$ describes the time derivative following the fluid element, while $d/dt = \partial/\partial t + [\mathbf{v} \cdot \nabla]$ represents the time derivative following the Lagrangian particle. The drag force F_D exerted on a superellipsoidal particle moving in a fluid is obtained using (Štrákl et al., 2022a):

$$F_D = \int_{\Gamma} t d\Gamma = \pi \rho_f \nu_f c \mathbf{K} \cdot [\mathbf{u} - \mathbf{v}], \quad (5)$$

where $t = \sigma \cdot \mathbf{n}$ denotes the boundary traction. To relate the coefficients \mathbf{K} and \mathbf{K}' of the resistance tensor in the inertial (iFoR) and in the particle frame of reference (pFoR), the rotation matrix \mathbf{R} is used:

$$\mathbf{K} = \mathbf{R}^T \mathbf{K}' \mathbf{R}. \quad (6)$$

To estimate the importance of the different force terms presented in Eq. (4), we rewrite Eq. (4) in non-dimensional form using L_0 and u_0 , which denote the characteristic scales of the problem and fluid velocity, respectively, (Cui et al., 2018b). Using the non-dimensional parameters $\mathbf{v}^* = \mathbf{v}/u_0, \mathbf{u}^* = \mathbf{u}/u_0, t^* = tu_0/L_0$ we write:

$$\frac{d\mathbf{v}^*}{dt^*} = \frac{A}{St} \left[\mathbf{v}^* + \frac{c}{3d_{eq}} \mathbf{K} \cdot [\mathbf{u}^* - \mathbf{v}^*] \right] + \frac{3}{2} R \frac{\partial \mathbf{u}^*}{\partial t^*} + R \left[[\mathbf{u}^* + \frac{1}{2} \mathbf{v}^*] \cdot \nabla \right] \mathbf{u}^*. \quad (7)$$

Moreover, we can separate the spherical and non-spherical contributions to the drag and write:

$$\frac{d\mathbf{v}^*}{dt^*} = \frac{A}{St} \left[\mathbf{v}^* + [\mathbf{u}^* - \mathbf{v}^*] + \left[\frac{c}{3d_{eq}} \mathbf{K} - \mathbf{I} \right] \cdot [\mathbf{u}^* - \mathbf{v}^*] \right] + \frac{3}{2} R \frac{\partial \mathbf{u}^*}{\partial t^*} + R \left[[\mathbf{u}^* + \frac{1}{2} \mathbf{v}^*] \cdot \nabla \right] \mathbf{u}^*, \quad (8)$$

where \mathbf{I} denotes the identity tensor. Using the non-dimensional Eq. (7)–(8) it can be seen that the importance of gravity and drag force scale with the factor A/St , while the pressure gradient and added mass term scale with the factor R , (Cui et al., 2018b). In this context, the nondimensional parameters A and R are depending on the fluid-particle ratio and are obtained as follows (Cui et al., 2018b):

$$R = \frac{\rho_f}{\rho_p + 0.5\rho_f}, \quad A = \frac{\rho_p}{\rho_p + 0.5\rho_f}. \quad (9)$$

In addition, St denotes the Stokes number, which describes the ratio of the characteristic particle response time τ_p to a characteristic time of the flow τ_f . The Stokes number of a particle with volume equivalent sphere diameter d_{eq} is obtained as follows:

$$St = \frac{\tau_p}{\tau_f} = \frac{\rho_p}{\rho_f} \frac{d_{eq}^2 u_0}{18 \nu_f L_0}. \quad (10)$$

The characteristic time scales of the particle τ_p and the flow τ_f are given by:

$$\tau_p = \frac{\rho_p}{\rho_f} \frac{d_{eq}^2}{18\nu_f}, \quad \tau_f = \frac{L_0}{u_0}. \quad (11)$$

Note that the pressure gradient and added mass force can be considered negligible compared to the reduced gravity and drag force if $\rho_p \gg \rho_f$ and thus $R \ll 1$, see Eq. (9), (Cui et al., 2018b). However, even if $\rho_p \approx \rho_f$, the impact of the additional forces can be considered minor compared to F_{GB} and F_D if the Stokes number is sufficiently small ($St \ll 1$) and consequently $A/St \gg 1$, see Eq. (9)–(10).

The particle Reynolds number is defined as follows:

$$Re_p = \frac{d_{eq} |u_{rel}|}{\nu_f}, \quad (12)$$

where $u_{rel} = u - v$ denotes the relative velocity between the particle v and the fluid u . The terminal velocity of a particle is reached when the sum of the flow-induced frictional and the buoyant forces on the particle balances the gravitational force F_D . In case of a spherical particle settling in Stokes flow the terminal velocity v_T is given by (Lamb, 1994):

$$v_T = \frac{d_{eq}^2}{18\nu_f} \frac{\rho_p - \rho_f}{\rho_f} g. \quad (13)$$

The kinematics of translational motion is given by:

$$\begin{bmatrix} dx/dt \\ dy/dt \\ dz/dt \end{bmatrix} = \mathbf{v}, \quad (14)$$

where the particle velocity is denoted as \mathbf{v} and the particle position as $\mathbf{x} = [x, y, z]^T$.

2.2.2. Dynamics of rotational motion

The rotational motion of an arbitrarily shaped particle moving in a fluid can be described in the pFoR as follows:

$$T_{x'} = I_{x'} \frac{d\omega_{x'}}{dt} - \omega_{y'}\omega_{z'} [I_{y'} - I_{z'}], \quad (15)$$

$$T_{y'} = I_{y'} \frac{d\omega_{y'}}{dt} - \omega_{z'}\omega_{x'} [I_{z'} - I_{x'}], \quad (16)$$

$$T_{z'} = I_{z'} \frac{d\omega_{z'}}{dt} - \omega_{x'}\omega_{y'} [I_{x'} - I_{y'}], \quad (17)$$

where $I_{x'}$, $I_{y'}$, $I_{z'}$ are the particle moments of inertia about the principal axes (the principal values of the particle's inertia tensor). Moreover, $T_{x'}$, $T_{y'}$, $T_{z'}$ and $\omega_{x'}$, $\omega_{y'}$, $\omega_{z'}$ denote the hydrodynamic torques on the particle and the particle angular velocities with respect to the principal axes. The moments of inertia for a superellipsoidal particle can be obtained as follows (Jaklič et al., 2000):

$$I_{x'} = \frac{1}{2} \rho abc \epsilon_1 \epsilon_2 \left[b^2 B \left(1.5\epsilon_2, \frac{\epsilon_2}{2} \right) B \left(\frac{\epsilon_1}{2}, 2\epsilon_1 + 1 \right) + 4c^2 B \left(\frac{\epsilon_2}{2}, \frac{\epsilon_2}{2} + 1 \right) B \left(1.5\epsilon_1, \epsilon_1 + 1 \right) \right], \quad (18)$$

$$I_{y'} = \frac{1}{2} \rho abc \epsilon_1 \epsilon_2 \left[a^2 B \left(1.5\epsilon_2, \frac{\epsilon_2}{2} \right) B \left(\frac{\epsilon_1}{2}, 2\epsilon_1 + 1 \right) + 4c^2 B \left(\frac{\epsilon_2}{2}, \frac{\epsilon_2}{2} + 1 \right) B \left(1.5\epsilon_1, \epsilon_1 + 1 \right) \right], \quad (19)$$

$$I_{z'} = \frac{1}{2} \rho abc \epsilon_1 \epsilon_2 \left[a^2 + b^2 \right] \left[B \left(1.5\epsilon_2, \frac{\epsilon_2}{2} \right) B \left(\frac{\epsilon_1}{2}, 2\epsilon_1 + 1 \right) \right]. \quad (20)$$

Taking both rotational and shear flow contributions into account, the torque can be expressed as (Štrákl et al., 2022a):

$$\mathbf{T} = \int_{\Gamma} \mathbf{r} \times t d\Gamma \hat{=} \pi \mu c^3 \left[\mathbf{\Pi}' \begin{bmatrix} f' \\ g' \\ h' \end{bmatrix} + \mathbf{\Omega}' \begin{bmatrix} \xi' - \omega_{x'} \\ \eta' - \omega_{y'} \\ \chi' - \omega_{z'} \end{bmatrix} \right], \quad (21)$$

where $\mathbf{\Omega}'$ is the coefficient matrix of the rotation resistance tensor and $\mathbf{\Pi}'$ the coefficient matrix of the deformation resistance tensor. In addition, f' , g' , h' denote the off-diagonal elements of the deformation rate tensor and ξ' , η' and χ' are spin tensor components, which are given by

$$f' = \frac{1}{2} \left[\frac{\partial u_{z'}}{\partial y} + \frac{\partial u_{y'}}{\partial z} \right], \quad g' = \frac{1}{2} \left[\frac{\partial u_{x'}}{\partial z} + \frac{\partial u_{z'}}{\partial x} \right], \quad h' = \frac{1}{2} \left[\frac{\partial u_{x'}}{\partial y} + \frac{\partial u_{y'}}{\partial x} \right], \quad (22)$$

$$\xi' = \frac{1}{2} \left[\frac{\partial u_{z'}}{\partial y} - \frac{\partial u_{y'}}{\partial z} \right], \quad \eta' = \frac{1}{2} \left[\frac{\partial u_{x'}}{\partial z} - \frac{\partial u_{z'}}{\partial x} \right], \quad \chi' = \frac{1}{2} \left[\frac{\partial u_{y'}}{\partial x} - \frac{\partial u_{x'}}{\partial y} \right]. \quad (23)$$

The orientation of particles in space can be parameterized by Euler angles $[\phi, \theta, \psi]$. However, this leads to a singularity for $\theta = 0$ and $\theta = \pi$. To overcome this drawback, the orientation in space is described by Euler parameters $\mathbf{e} = [e_0, e_1, e_2, e_3]$. The Euler parameters (quaternions) can be determined using:

$$\mathbf{e} = \begin{bmatrix} e_0 \\ e_1 \\ e_2 \\ e_3 \end{bmatrix} = \begin{bmatrix} \cos [0.5 [\phi + \psi]] \cos [\theta/2] \\ \cos [0.5 [\phi - \psi]] \sin [\theta/2] \\ \sin [0.5 [\phi - \psi]] \sin [\theta/2] \\ \sin [0.5 [\phi + \psi]] \cos [\theta/2] \end{bmatrix} \quad (24)$$

and are subject to the constraint $e_0^2 + e_1^2 + e_2^2 + e_3^2 = 1$, (Goldstein, 1980). The rotation matrix in the inertia frame follows as

$$\mathbf{R} = \begin{bmatrix} e_0^2 + e_1^2 - e_2^2 - e_3^2 & 2[e_1 e_2 + e_0 e_3] & 2[e_1 e_3 - e_0 e_2] \\ 2[e_1 e_2 - e_0 e_3] & e_0^2 - e_1^2 + e_2^2 - e_3^2 & 2[e_2 e_3 - e_0 e_1] \\ 2[e_1 e_3 + e_0 e_2] & 2[e_2 e_3 - e_0 e_1] & e_0^2 - e_1^2 - e_2^2 + e_3^2 \end{bmatrix}. \quad (25)$$

In addition, the evolution of the quaternions (Euler parameters) is related to the angular particle velocity in the particle frame ω' as:

$$\begin{bmatrix} de_0/dt \\ de_1/dt \\ de_2/dt \\ de_3/dt \end{bmatrix} = \frac{1}{2} \begin{bmatrix} -e_1 & -e_2 & -e_3 \\ e_0 & -e_3 & e_2 \\ e_3 & e_0 & -e_1 \\ -e_2 & e_1 & e_0 \end{bmatrix} \omega'. \quad (26)$$

2.2.3. Superellipsoid surrogate approach

In the case of the targeted microparticles the flow around the particles can be described by the Stokes flow, for which Happel and Brenner (1983) found that the translational and rotational resistance tensors are symmetric. Therefore, each particle has principal translation axes, i.e. three perpendicular directions. Consequently, if a particle is translated without rotation in one of those, it experiences a force solely in that direction, (Štrákl et al., 2022a). In the case of an orthotropic particle and the choice of pFoR in line with the symmetry planes, the resistance matrices for translation \mathbf{K}' , rotation $\mathbf{\Omega}'$ and deformation $\mathbf{\Pi}'$ are diagonal, (Štrákl et al., 2022a). In our previous work, see Štrákl et al. (2022a), we developed a superellipsoid surrogate approach for \mathbf{K}' , $\mathbf{\Omega}'$ and $\mathbf{\Pi}'$ for superellipsoids with shapes in the following parameter ranges: $\lambda_1 = [1, 11]$, $\lambda_2 = [1, 11]$, $\epsilon_1 = [0.2, 1.8]$ and $\epsilon_2 = [0.2, 1.8]$. In this context, we performed a parametric study to model the shape dependence of the components of the translation, rotation, and deformation resistance tensor.

The approach, (Štrákl et al., 2022a), was set up by deriving a multivariate approximation procedure to predict the tensor coefficients \mathbf{K}' , $\mathbf{\Omega}'$, and $\mathbf{\Pi}'$ individually. We introduced m th order univariate polynomials in the form $p_m(x) = [1 \ x \ x^2 \ \dots \ x^m]^T$, which were employed for each geometric parameter, i.e. $p_3(\lambda_1)$, $p_3(\lambda_2)$ with $m = 3$ and $p_2(\epsilon_1)$, $p_2(\epsilon_2)$ using $m = 2$. Furthermore, we combined the polynomials of the aspect ratio and shape factors as $p_{3,3}(\lambda_1, \lambda_2) = \text{vec} \left([p_3(\lambda_1) p_3(\lambda_2)]^T \right)$ and $p_{2,2}(\epsilon_1, \epsilon_2) = \text{vec} \left([p_2(\epsilon_1) p_2(\epsilon_2)]^T \right)$. Finally, we determined the resulting approximation scheme in the form of a multivariate polynomial as follows (Štrákl et al., 2022a):

$$f(\lambda_1, \lambda_2, \epsilon_1, \epsilon_2) = p_{3,3}(\lambda_1, \lambda_2)^T \hat{\mathbf{A}} p_{2,2}(\epsilon_1, \epsilon_2), \quad (27)$$

with f approximating one of the components of one of the resistance matrices. The coefficients of $\hat{\mathbf{A}}$ were determined using an optimization problem for each tensor component given by Štrákl et al. (2022a):

$$\min_{\hat{\mathbf{A}}} \sum_{i=1}^n \left[\frac{f_i(\lambda_1, \lambda_2, \epsilon_1, \epsilon_2) - y_i}{y_i} \right]^2, \quad (28)$$

where $f_i(\lambda_1, \lambda_2, \epsilon_1, \epsilon_2)$ denotes the approximation result for each individual tensor component for the i th particle. Moreover, y_i labels the tensor component of the i th particle shape and n denotes the number of particle shapes considered. The determined coefficients of $\hat{\mathbf{A}}$ are given in Štrákl et al. (2022a) (available on Github Štrákl et al., 2022b). Moreover, the fitting accuracy of the surrogate model was increased by dividing it into two subdomains, namely \mathcal{R}_1 for $\lambda_1 \leq 5$ and \mathcal{R}_2 for $11 \leq \lambda_1 < 5$. As a result of the optimization problem, we obtain the polynomial coefficient matrices with the best fitting terms for each tensor component in both ranges which exemplarily renders $\hat{\mathbf{A}}_{\mathcal{R}_1}(K'_{xx})$, $\hat{\mathbf{A}}_{\mathcal{R}_1}(K'_{yy})$, $\hat{\mathbf{A}}_{\mathcal{R}_1}(K'_{zz})$ and $\hat{\mathbf{A}}_{\mathcal{R}_2}(K'_{xx})$, $\hat{\mathbf{A}}_{\mathcal{R}_2}(K'_{yy})$, $\hat{\mathbf{A}}_{\mathcal{R}_2}(K'_{zz})$ considering the translational resistance matrix \mathbf{K}' .

2.3. Wall interception model

As described by Feng and Kleinstreuer (2013), non-spherical particles such as ellipsoids and fibers show more complicated deposition behavior than spheres. For spherical particles, wall contact occurs when the distance between the particle centroid \mathbf{r}_c and the nearest wall point \mathbf{r}_w is less than or equal to the particle radius, i.e. $\|\mathbf{r}_c - \mathbf{r}_w\|_2 \leq d_p/2$. Furthermore, for sticky walls, e.g. mucus-coated airways, wall deposition is assumed when there is contact between the particle and the wall, (Feng and Kleinstreuer, 2013). In contrast to spherical particles, deciding whether non-spherical particles deposit is more complicated as there are three different possibilities (Feng and Kleinstreuer, 2013):

1. if $\|\mathbf{r}_c - \mathbf{r}_w\|_2 \leq c$, the particle will deposit.
2. if $\|\mathbf{r}_c - \mathbf{r}_w\|_2 > a$, the particle does not touch the wall.
3. if $c < \|\mathbf{r}_c - \mathbf{r}_w\|_2 \leq a$, the particle deposits depending on its orientation.

Note that c labels the smallest half axis and a the major half axis of the superellipsoidal particle under consideration. In the following, we present the deposition algorithm for the 3rd case, i.e. $c < \|\mathbf{r}_c - \mathbf{r}_w\|_2 \leq a$. In this context, we introduce the equation of the wall.

Let $\hat{\mathbf{h}}, \hat{\mathbf{j}}, \hat{\mathbf{k}}$ be three points on a plane wall in a frame of reference with origin at the wall. The corresponding wall normal can then be determined as follows:

$$\mathbf{n} = \frac{[\hat{\mathbf{k}} - \hat{\mathbf{h}}] \times [\hat{\mathbf{j}} - \hat{\mathbf{h}}]}{[\hat{\mathbf{k}} - \hat{\mathbf{h}}] \times [\hat{\mathbf{j}} - \hat{\mathbf{h}}]}, \quad (29)$$

leading to the wall equation:

$$W(\mathbf{r}) = \mathbf{n} \cdot [\mathbf{r} - \hat{\mathbf{h}}] = 0, \quad (30)$$

where $\mathbf{r} = [x, y, z]^T$ denotes an arbitrary wall point. Note that in the context of this work, an established particle-wall contact is treated as particle deposit. The algorithm for detecting particle-wall contact (Algorithm 1) is presented below (You and Zhao, 2018).

3. Validation

In the following, we consider three different validation cases, i.e. particles in a lid driven cavity flow, a pipe flow, and a simplified bifurcation. In this framework, we assume steady-state flow conditions as well as a one-way coupling of particle and fluid flow, i.e. the influence of the particles on the laminar flow of an incompressible fluid under consideration is neglected. Moreover, the flow is considered laminar, since the Reynolds number is sufficiently low in all cases studied and particle-particle interactions are neglected as we assume dilute particle flow. To obtain the time evolution of the particle trajectory, the numerical solution of the momentum equations (Eq. ((4),(15)-(17))) and the kinematics equations (Eq. (26)-(14)) are required.

Algorithm 1 Wall deposition model

```

forall particles do
  forall wall faces in interaction distance do
    if  $\|\mathbf{r}_c - \mathbf{r}_w\|_2 \leq c$ : contact to wall
    if  $\|\mathbf{r}_c - \mathbf{r}_w\|_2 > a$ : no contact to wall
    if  $c < \|\mathbf{r}_c - \mathbf{r}_w\|_2 \leq a$ :
      Map wall data to positive octant of superellipsoid surface  $S$ 
      Find  $\mathbf{r}$  by solving optimization problem:  $\min(S(\mathbf{r}))$  with the
      constraint  $W(\mathbf{r}) = 0$ 
      if  $S(\mathbf{r}) \leq 1.0$ : particle-wall contact  $\rightarrow$  particle deposits.
    end
  end

```

3.1. Flow field

Since we use a one-way coupling of fluid and particle, a priori numerical calculation of the steady-state flow field is required for Lagrangian particle tracking. In this work, the Euler frame is used to solve the flow field. We obtain the incompressible steady-state flow by applying the Navier Stokes equations using OpenFOAM[®], (OpenFOAM The OpenFOAM Foundation, 2020; Weller et al., 1998). The governing equations are given by (Weller et al., 1998):

$$\text{div}(\rho_f \mathbf{u} \otimes \mathbf{u}) = -\text{grad}p + \text{div}\boldsymbol{\tau} + \mathbf{f}_D \quad (31)$$

and

$$\text{div}\mathbf{u} = 0. \quad (32)$$

The viscous stress tensor $\boldsymbol{\tau}$ is obtained by (Ferziger and Perić, 2008):

$$\boldsymbol{\tau} := \mu \text{grad}^{\text{SYM}}\mathbf{u}. \quad (33)$$

OpenFOAM[®] uses the finite volume method (FVM) to discretize the above equations. In Eqs. (31)–(33), \mathbf{u} , p and ρ_f denote the fluid velocity, pressure and fluid density, respectively. Moreover, body forces are captured by \mathbf{f}_D .

3.2. Reference analytical model

To validate the developed superellipsoid particle tracking algorithm, we replicate numerical and experimental studies, which employed spheres and prolate ellipsoids. These particles correspond to superellipsoids with $\lambda_1 = \lambda_2 = \epsilon_1 = \epsilon_2 = 1.0$ and $\lambda_1 > \lambda_2 = \epsilon_1 = \epsilon_2 = 1.0$, respectively. For prolate ellipsoidal particles the tensor coefficients \mathbf{K}' , $\boldsymbol{\Pi}'$ and $\boldsymbol{\Omega}'$ can be determined analytically and are functions of the particle aspect ratio ($\lambda = \lambda_1$). Followingly, the coefficients \mathbf{K}' can be written as:

$$K'_{yy} = K'_{zz} = \frac{16 [\lambda^2 - 1]^{3/2}}{[2\lambda^2 - 3] \ln(\lambda + \sqrt{\lambda^2 - 1}) + \lambda \sqrt{\lambda^2 - 1}}, \quad (34)$$

$$K'_{xx} = \frac{8 [\lambda^2 - 1]^{3/2}}{[2\lambda^2 - 1] \ln(\lambda + \sqrt{\lambda^2 - 1}) - \lambda \sqrt{\lambda^2 - 1}}, \quad (35)$$

In the limit of a spherical particle shape the resistance matrix is given by

$$\lim_{\lambda \rightarrow 1} \mathbf{K}' = 6 \mathbf{I}, \quad (36)$$

where \mathbf{I} denotes the identity matrix, leading to $K_{xx} = K_{yy} = K_{zz} = 6$. The tensor coefficients $\boldsymbol{\Pi}'$ and $\boldsymbol{\Omega}'$ can be obtained as follows:

$$\boldsymbol{\Pi}' = \frac{16}{3} \lambda [1 - \lambda^2] \begin{bmatrix} 0 \\ \frac{1}{\beta_0 + \lambda^2 \gamma_0} \\ -1 \\ \frac{1}{\alpha_0 + \lambda^2 \gamma_0} \end{bmatrix}, \quad (37)$$

Table 1
 \mathbf{K}' , $\mathbf{\Omega}'$, $\mathbf{\Pi}'$ tensor coefficients obtained analytically (A) or by using the superellipsoid surrogate approach proposed by Štrákl et al. (2022a) (B).

λ		K'_{xx}	K'_{yy}	K'_{zz}	Π'_{xx}	Π'_{yy}	Π'_{zz}	Ω'_{xx}	Ω'_{yy}	Ω'_{zz}
1.0	A	6	6	6	0	0	0	8	8	8
	B	6.00	6.00	6.00	0.00	0.00	0.00	7.98	7.98	7.97
2.0	A	7.22	8.27	8.27	0.00	-14.45	14.45	12.91	24.08	24.08
	B	7.22	8.28	8.28	0.003	-14.44	14.43	12.83	24.01	23.99
5.0	A	10.71	14.225	14.23	0.00	-171.34	171.34	28.24	185.62	185.62
	B	10.70	14.23	14.24	0.02	-171.08	170.85	27.91	185.15	184.95

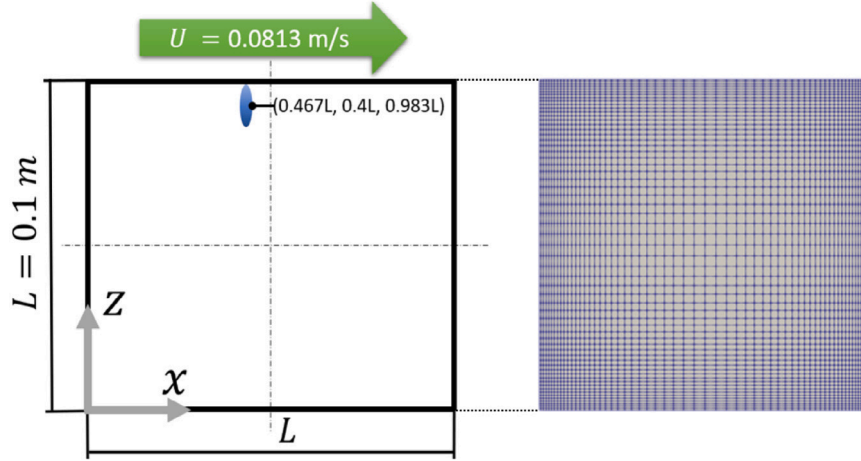


Fig. 2. Sketch of computational domain of the lid driven cavity case and particle injection position in the $y/L = 0.4$ plane.

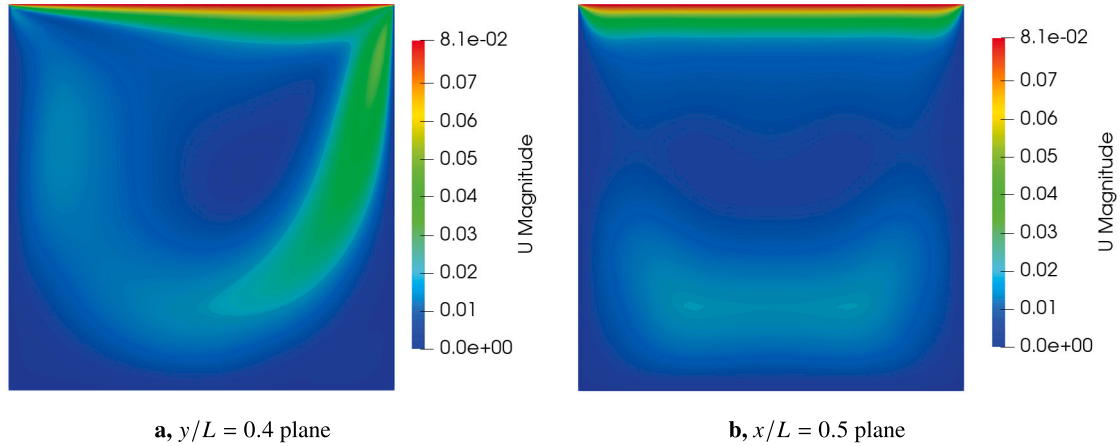


Fig. 3. Flow field inside the lid driven cavity in the $y/L = 0.4$ and $x/L = 0.5$ plane ($Re = 470$).

$$\mathbf{\Omega}' = \frac{16\lambda}{3} \begin{bmatrix} \frac{2}{[\alpha_0 + \beta_0]} \\ \frac{1}{[\beta_0 + \lambda^2 \gamma_0]} [1 + \lambda^2] \\ \frac{1}{[\alpha_0 + \lambda^2 \gamma_0]} [1 + \lambda^2] \end{bmatrix} \quad (38)$$

by using the non-dimensional coefficients α_0 , β_0 and γ_0 defined by Gallily and Cohen (1979):

$$\alpha_0 = \beta_0 = \frac{\lambda^2}{\lambda^2 - 1} + \frac{\lambda}{2[\lambda^2 - 1]^{3/2}} \ln \left[\frac{\lambda - \sqrt{\lambda^2 - 1}}{\lambda + \sqrt{\lambda^2 - 1}} \right], \quad (39)$$

$$\gamma_0 = -\frac{2}{\lambda^2 - 1} - \frac{\lambda}{[\lambda^2 - 1]^{3/2}} \ln \left[\frac{\lambda - \sqrt{\lambda^2 - 1}}{\lambda + \sqrt{\lambda^2 - 1}} \right]. \quad (40)$$

In the limit of spherical particle shape ($\lambda_1 = \lambda_2 = \epsilon_1 = \epsilon_2 = 1.0$) the nondimensional coefficients render $\alpha_0 = \beta_0 = \lambda\gamma_0 = 2/3$, leading to $\Omega'_{xx} = \Omega'_{yy} = \Omega'_{zz} = 8$ and $\Pi'_{xx} = \Pi'_{yy} = \Pi'_{zz} = 0$.

3.3. Lid driven cavity

The lid-driven cavity flow is a common reference case for viscous incompressible fluid flows, (Cui et al., 2018b). It has been extensively studied by both experimental, (Tsorng et al., 2008; Koseff and Street, 1984), analytical, (Shankar and Deshpande, 2000), and numerical methods, (Chiang and Sheu, 1997; Cui et al., 2018b). Nevertheless, there are few studies on the particle motion of non-spherical particles in lid-driven cavity flows, (Cui et al., 2018b). Tsorng et al. (2008) used data from video images to investigate the motion of macroscopic rigid spheres moving in a 3D viscous flow in a closed cubic cavity in the $y/L \approx 0.4$ plane. Tsorng et al. (2008) employed spherical macro-particles with $d_p = 3$ mm and $\rho_p = 1210$ kg/m. In addition, Cui et al. (2018b) studied prolate ellipsoidal particles moving in the cavity flow employing the same setup as Tsorng et al. (2008).

The flow conditions used in the following are consistent with the numerical study of Cui et al. (2018b). Fig. 2 sketches the computational

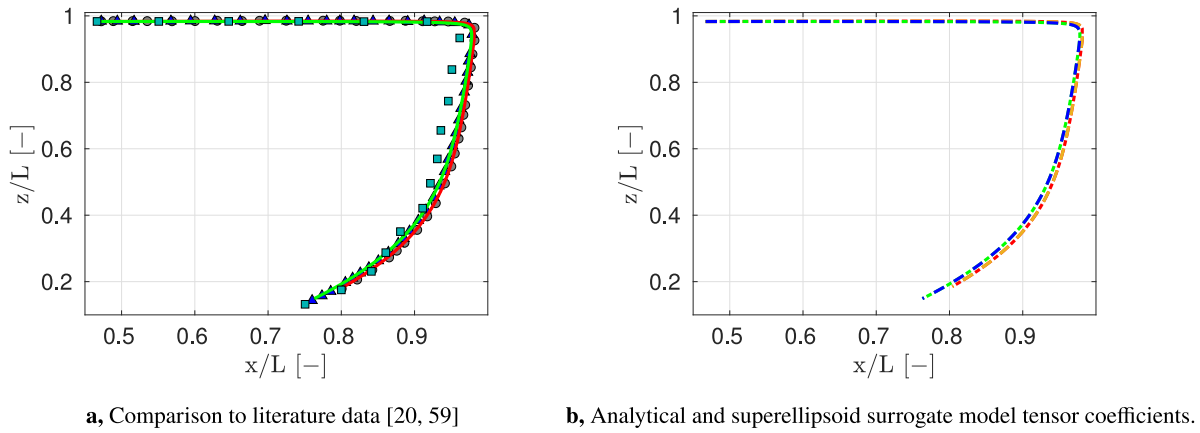


Fig. 4. Trajectory of spherical particle in the $y/L = 0.4$ plane: — Present model $\rho^* = [\rho_f - \rho_p]/\rho_f = -0.07\%$ (analytical coefficients), — Present model $\rho^* = 0.05\%$ (analytical coefficients), ■ Present model $\rho^* = -0.07\%$ (superellipsoid surrogate approach Štrákl et al., 2022a), ■ Present model $\rho^* = 0.05\%$ (superellipsoid surrogate approach Štrákl et al., 2022a), ■ Tsornig et al. ($\rho^* = 0.05\%$) (Tsornig et al., 2008), ▲ Cui et al. ($\rho^* = -0.07\%$) (Cui et al., 2018b), ● Cui et al. ($\rho^* = 0.05\%$) (Cui et al., 2018b).

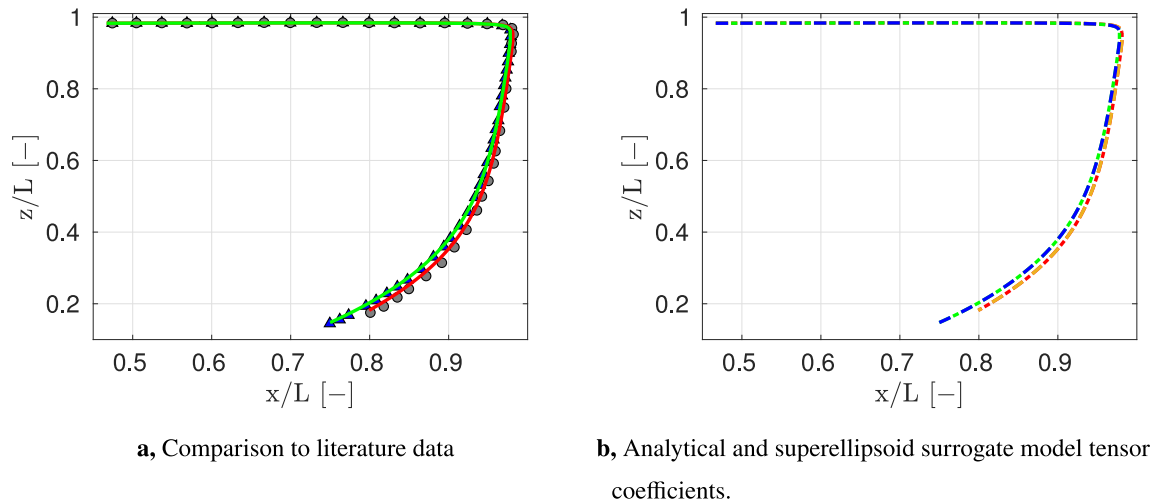


Fig. 5. Trajectory of prolate ellipsoidal particles in the $y/L = 0.4$ plane: — Present model $\lambda = 5$ ($\rho^* = 0.05\%$, analytical coefficients), — Present model $\lambda = 2$ ($\rho^* = 0.05\%$, analytical coefficients), ■ Present model $\lambda = 5$ ($\rho^* = 0.05\%$, superellipsoid surrogate approach (Štrákl et al., 2022a)), ■ $\lambda = 2$ ($\rho^* = 0.05\%$, superellipsoid surrogate approach Štrákl et al., 2022a), ▲ Cui et al. $\lambda = 5$ ($\rho^* = 0.05\%$, Cui et al., 2018b), ● Cui et al. $\lambda = 2$ ($\rho^* = 0.05\%$, Cui et al., 2018b).

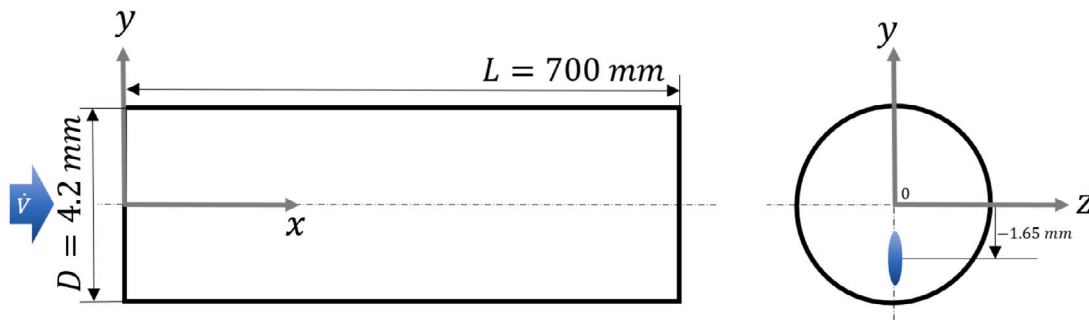


Fig. 6. Sketch of the circular tube and initial position of the particle in the cross-section.

domain with an edge length of $L = 0.1$ m. The shear flow in the cavity is caused by a constant velocity $U = 0.0813$ m/s of the moving top wall. Using a kinematic viscosity of the fluid $\nu_f = 17.3$ mm²/s results in a Reynolds number of $Re = 470$. In addition, the front and rear walls are assumed to be symmetry boundaries. Moreover, all remaining walls are described as no-slip boundaries. Besides, the computational grid for the fluid domain is discretized with a grid resolution of $60 \times 60 \times 60$ cells. Fig. 2 graphically illustrates the particle tracking approach within the cavity, highlighting the initial position

and orientation of the injected particle. Note that we consider both drag force F_D and reduced gravitational force F_{GB} . The particles considered in this validation are listed in Table 1.

In addition, Fig. 3 presents the velocity distribution within the lid-driven cavity at $Re = 470$ in the $y/L = 0.4$ and $x/L = 0.5$ planes. The flow is driven by moving the upper boundary, which causes a large primary vortex visible in the $y/L = 0.4$ plane, see Fig. 3(a).

In the first step, we validate the superellipsoid particle tracking for the limiting case of a spherical shape. For this purpose, we choose the

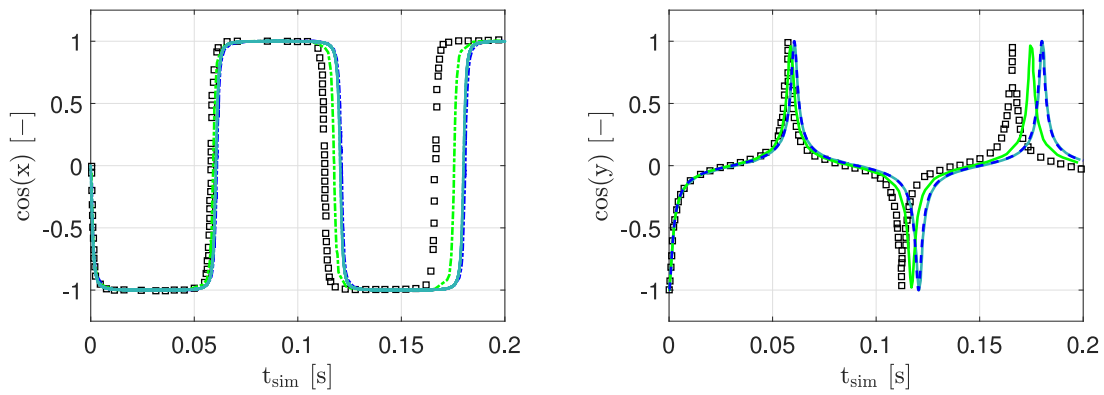


Fig. 7. Comparison of direction cosines of prolate ellipsoids in pipe flow: □ Tian et al. (2012), — ($U_{max} = 1.0$ m/s) (Cui et al., 2018b), — ($U_{max} = 0.97$ m/s) (Cui et al., 2018b), ■ present superellipsoid particle tracking using the reference analytical model ($U_{max} = 0.97$ m/s).


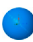



Table 2

Analytical \mathbf{K}' , $\mathbf{\Omega}'$ and $\mathbf{\Pi}'$ tensor coefficients for three prolate ellipsoidal particles as well as approximations according to the superellipsoid surrogate approach of Štrákl et al. (2022a).

Coeff. \mathbf{K}' , $\mathbf{\Omega}'$, $\mathbf{\Pi}'$	Prolate ellipsoids					
	$\lambda = 3.5$		$\lambda = 7.0$		$\lambda = 14.0$	
	Analytical	Fit (Štrákl et al., 2022a)	Analytical	Fit (Štrákl et al., 2022a)	Analytical	Fit (Štrákl et al., 2022a)
K_{xx}	9.01	9.01	12.85	12.85	19.68	19.83
K_{yy}	11.36	11.37	17.81	17.83	29.22	29.41
K_{zz}	11.36	11.38	17.81	17.85	29.22	29.54
Ω_{xx}	20.50	20.33	38.67	38.28	75.57	76.02
Ω_{yy}	79.61	79.42	428.43	427.72	2584.71	2590.33
Ω_{zz}	79.61	79.37	428.43	427.15	2584.71	2583.41
Π_{xx}	0.00	-0.001	0.0	0.01	0.0	0.31
Π_{yy}	-67.59	-67.53	-411.29	-410.79	-2558.47	-2564.16
Π_{zz}	67.59	67.48	411.29	409.86	2558.47	2540.22
$x_{Diff,yy} = \frac{ \Omega_{yy}' - \Pi_{yy}' }{ \Pi_{yy}' }$ [%]	17.78	17.61	4.17	4.12	1.03	1.02
$x_{Diff,zz} = \frac{ \Omega_{zz}' - \Pi_{zz}' }{ \Pi_{zz}' }$ [%]	17.78	17.62	4.17	4.22	1.03	1.70

Table 3

\mathbf{K}' , $\mathbf{\Omega}'$ and $\mathbf{\Pi}'$ tensor coefficients estimations for a realistic pollen particle (Štrákl et al., 2022a), obtained via DNS, approximated via sphere, prolate ellipsoid, triaxial ellipsoid and superellipsoid.

\mathbf{K}' , $\mathbf{\Omega}'$, $\mathbf{\Pi}'$	Pollen ^a (Štrákl et al., 2022a)	Sphere ^b	Prolate ^c	Triaxial ^d	Superel. ^e	Shape factors		
						Haider and Levenspiel (1989)	Leith (1987)	Hölzer and Sommerfeld (2008)
Case ID	–	A	B	C	D1/D2	E1/E2	F1/F2	G1/G2
K'_{xx}	10.7	6	7.235	9.413	10.58	9.505	9.324	9.922
K'_{yy}	10.80	6	8.293	9.582	10.71	9.505	9.431	9.968
K'_{zz}	12.01	6	8.293	10.84	11.86	9.505	10.36	10.46
Ω'_{xx}	50.07	8	12.95	34.05	0/47.23	0/8	0/8	0/8
Ω'_{yy}	50.88	8	24.29	37.65	0/50.71	0/8	0/8	0/8
Ω'_{zz}	63.20	8	24.29	44.79	0/61.65	0/8	0/8	0/8
Π'_{xx}	25.31	0	0.0	19.35	0/23.51	0/0	0/0	0/0
Π'_{yy}	-26.22	0	-14.63	-23.53	0/-27.56	0/0	0/0	0/0
Π'_{zz}	0.86	0	14.63	3.87	0/3.791	0/0	0/0	0/0
$K'_{xx} 2c/d_{eq}$	6.09	6	5.733	5.944	0/6.025	5.412	5.309	5.650
$K'_{yy} 2c/d_{eq}$	6.15	6	6.572	6.051	0/6.100	5.412	5.370	5.676
$K'_{zz} 2c/d_{eq}$	6.84	6	6.572	6.846	0/6.756	5.412	5.899	5.956

^aFitted tensor coefficients (Štrákl et al., 2022a) solely for comparison (superellipsoid surrogate approach not applicable due to non-symmetric particle shape).

^bAnalytical tensor coefficients for $\lambda_1 = \lambda_2 = \epsilon_1 = \epsilon_2 = 1.0$.

^cAnalytical tensor coefficients for $\lambda_1 = 2.009$; $\lambda_2 = \epsilon_1 = \epsilon_2 = 1.0$.

^dSuperellipsoid surrogate mode, I (Štrákl et al., 2022a), for $\lambda_1 = 2.081$; $\lambda_2 = 1.907$; $\epsilon_1 = \epsilon_2 = 1.0$.

^eSuperellipsoid surrogate approach, Štrákl et al. (2022a), for $\lambda_1 = 1.96$; $\lambda_2 = 1.83$; $\epsilon_1 = 0.564$; $\epsilon_2 = 0.472$.

numerical results of Cui et al. (2018b) and the experimental results of Tsoeng et al. (2008) as references. In agreement with Cui et al. (2018b), we consider two subcases, i.e. $\rho^* = [\rho_f - \rho_p]/\rho_f = -0.07\%$ (Case A) and $\rho^* = 0.05\%$ (Case B). Recall, that ρ_f denotes the fluid density, while ρ_p denotes the particle density. The particle response

time in the present study is $\tau_p = 0.029$ s and the particle Stokes number is $St = 0.023 \ll 1$. Fig. 4 displays the resulting trajectory of the superellipsoidal particle in the plane $y/L = 0.4$ next to the reference results, (Tsoeng et al., 2008; Cui et al., 2018b). As shown in Fig. 4, the present superellipsoid particle tracking is able to accurately

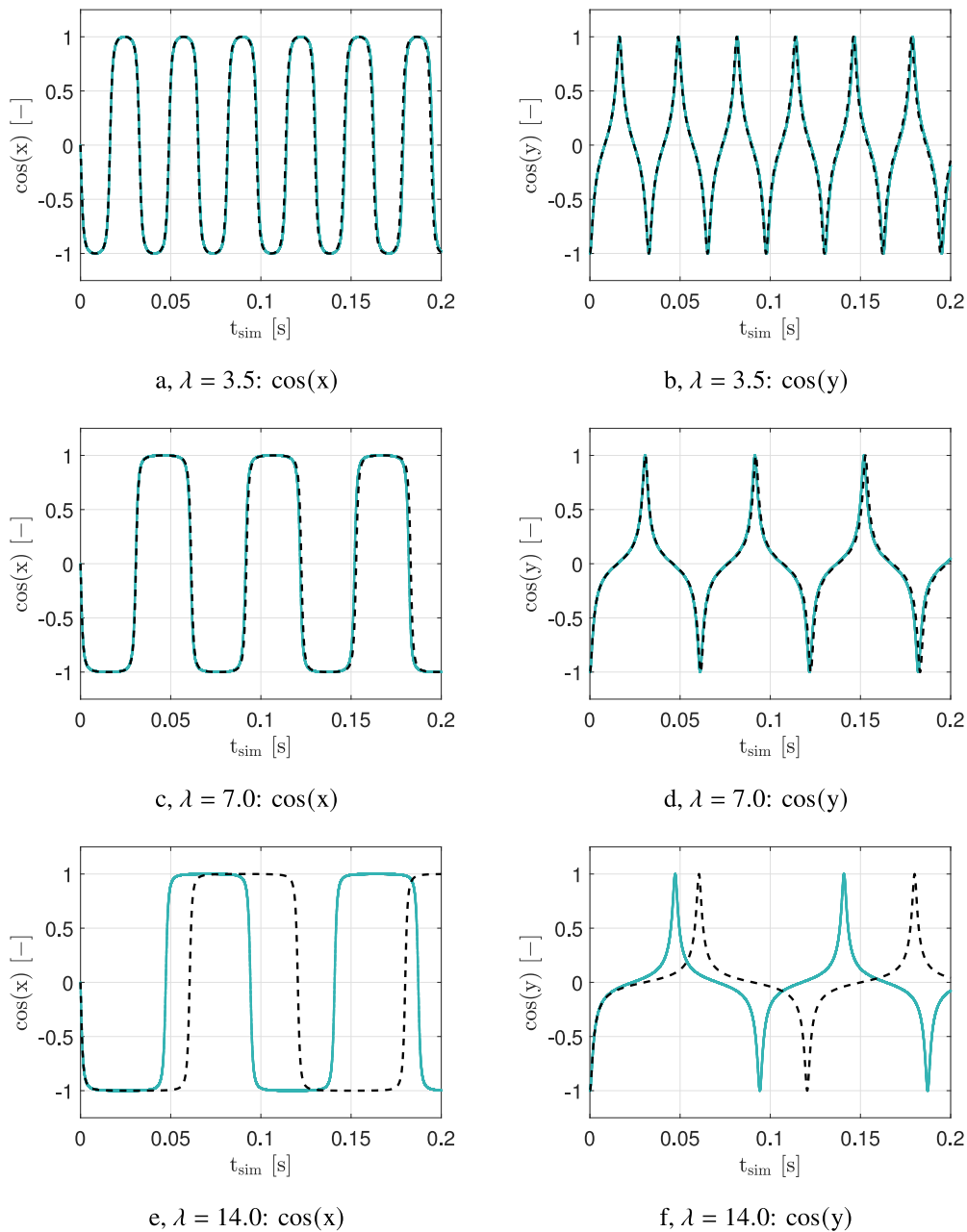


Fig. 8. Directional cosines of prolate ellipsoids in pipe flow: ■■ present superellipsoid particle tracking (analytical coefficients), ■ present superellipsoid particle tracking (using our superellipsoid surrogate approach, Štrákl et al. (2022a)).

reproduce the trajectory of the spherical particle under consideration, as the deviations from the numerical results of Cui et al. (2018b) are negligible. In addition, Fig. 5 (b) highlights the applicability of the superellipsoid surrogate approach, (Štrákl et al., 2022a), in the spherical limit, since the particle motion is identical compared to the use of the analytical tensor coefficients.

In the next step, we analyze the motion of prolate ellipsoids suspended in the lid driven cavity flow. In this context, we consider both prolate ellipsoids with $d_{eq} = 3$ mm and either $\lambda = 2.0$ or $\lambda = 5.0$. The initial orientation of the particles is illustrated in Fig. 2. The trajectories of the tracked prolates over a period of $t_{max} = 5$ s ($\approx 172.4\tau_p$) considering F_D and F_G are shown in Fig. 5. Fig. 5 (a) shows excellent agreement of the superellipsoid particle tracking with the numerical results for prolate ellipsoids presented by Cui et al. (2018b). In addition, the simulation is capable to capture the phenomenon that the elongated particles tend to move farther away from the right boundary wall as the

aspect ratio increases, (Cui et al., 2018b). Moreover, Fig. 5 (b) shows that the novel superellipsoid surrogate approach, presented in Štrákl et al. (2022a) yields virtually identical results compared to the simulation employing analytical resistance tensor coefficients. This validation case clearly demonstrates the applicability of the novel superellipsoid particle tracking together with the superellipsoid surrogate approach proposed by Štrákl et al. (2022a) to replicate spherical and ellipsoidal particle motion (up to $\lambda \leq 5$).

3.4. Pipe flow

Furthermore, we compare the novel superellipsoid particle tracking with numerical results presented by Tian et al. (2012) for tracking suspended ellipsoidal particles in a circular pipe flow. Tian et al. (2012) used a circular channel with length $L = 0.7$ m and diameter $D = 4.2$ mm. The considered pipe flow is laminar, since we assume

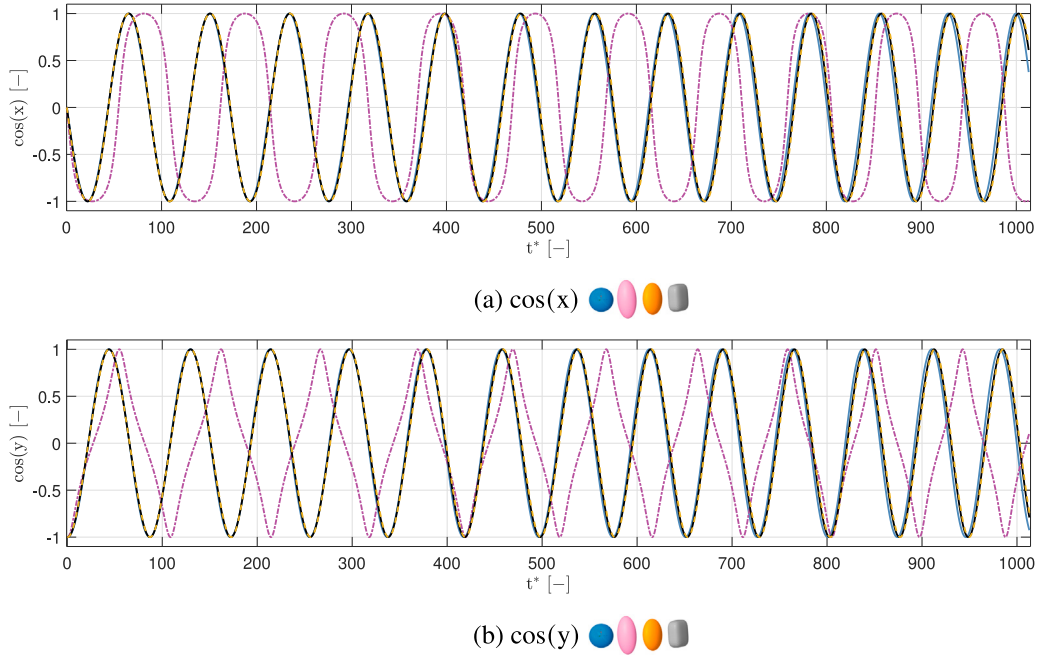


Fig. 9. Directional cosines of four different particle shapes in a laminar pipe flow. Non-dimensional parameter: $t^* = t_{Sim}/\tau_p$. Initial orientation $\varphi = -90^\circ$, $\theta = 0^\circ$, $\psi = 0^\circ$; ■ A (sphere), ■ B (prolate ellipsoid), ■ C (triaxial ellipsoid), ■ D2 (superellipsoid).

an average inflow velocity of $\bar{U} = 0.485$ m/s as suggested by Cui et al. (2018b). The particle under consideration has a prolate ellipsoidal shape with a semi-minor axis $c = 0.5$ μm , an aspect ratio $\lambda = 14.0$ and a density of $\rho_p = 2560$ kg/m^3 . Note that the air density is 1.208 kg/m^3 (thus $\rho_p \gg \rho_f$) and the kinematic viscosity is 1.491×10^5 mm^2/s rendering $\text{Re} = 137$. The particle response time renders $\tau_p = 0.046$ ms and the Stokes number is $\text{St} = 0.01$. The ellipsoid is positioned in the x - y plane with an initial position of $y = -1.65$ mm, as depicted in Fig. 6. The flow vorticity at the injection position is $\omega_f = 726.95$ rad/s .

The analytically determined tensor coefficients as well as the tensor coefficients obtained using our superellipsoid surrogate approach, (Štrákl et al., 2022a), are listed in Table 2. Note that the relative difference between the tensor coefficients Π'_{yy} and Ω'_{yy} ($x_{Diff,yy} = [|\Omega'_{yy}| - |\Pi'_{yy}|] / |\Pi'_{yy}|$) decreases with increasing λ , see Table 2. A similar trend is observed for the tensor coefficients Ω'_{zz} and Π'_{zz} .

Fig. 7 shows excellent agreement in the rotational pattern between the results of the present superellipsoid particle tracking (using the reference analytical model) and the results of Cui et al. (2018b). The phase differences between the results of Tian et al. (2012) and the results of Cui et al. (2018b) are attributed to density and viscosity differences as Tian et al. (2012) did not specify the air properties used. Consequently, a difference in density and viscosity leads to a slightly altered Stokes number considered in the simulations, (Cui et al., 2018b). However, it should be emphasized that the excellent agreement between the present simulation and the numerical results presented by Cui et al. (2018b) confirms the ability of our superellipsoid particle tracking to accurately capture the rotational motion of the studied non-spherical particle.

3.4.1. Analysis of different prolate ellipsoids in a laminar pipe flow

Having validated the superellipsoid particle tracking ability to replicate the results of Cui et al. (2018b) and Tian et al. (2012), using analytically determined \mathbf{K}' , $\mathbf{\Omega}'$, $\mathbf{\Pi}'$ tensor coefficients, we investigate the ability of the novel superellipsoid surrogate approach to model the resistance tensors of superellipsoidal particles as described in Štrákl et al. (2022a). Note that validation is possible in the prolate ellipsoid limit, since the resistance tensor coefficients can be determined analytically. In this context, we study the following aspect ratios: $\lambda =$

3.5, 7.0, 14.0 using $c = 0.5$ μm , rendering $\text{St} = 0.004$, 0.006 and 0.011, respectively. The tensor coefficients are listed in Table 2. To compare the rotational motion, we track the direction cosines of the particle axis with respect to the global reference system. The resulting directional cosines for the three prolate spheroids considered are shown in Fig. 8.

As presented in Fig. 8 (a–d), employing the novel superellipsoid surrogate approach of Štrákl et al. (2022a) or using the reference analytical model results in comparable particle rotation. However, as shown in Fig. 8 (e–f) our superellipsoid surrogate approach, (Štrákl et al., 2022a), renders a deviating rotational motion for strongly elongated particles, e.g. $\lambda = 14.0$, although the errors in prediction the resistance tensor coefficients are small, see Table 2. As presented in Fig. 8, we find that the relative differences between the tensor coefficients of $\mathbf{\Omega}'$ and $\mathbf{\Pi}'$ vanish as λ increases. This enables strongly elongated particles to align with the flow as the torque can cancel out ($T \approx 0$) due to similar $\mathbf{\Omega}'$ and $\mathbf{\Pi}'$ tensor coefficients, see Eq. (21). Therefore, even minor deviations in the tensor coefficients prediction for strongly elongated particles can lead to an increase in the relative difference of the tensor coefficients of $\mathbf{\Omega}'$ and $\mathbf{\Pi}'$, resulting in an earlier onset of rotation after alignment with the flow, as shown in Fig. 8 (e–f).

3.4.2. Analysis of various superellipsoids in pipe flow

In the next step, we attempt to approximate the dynamics of a realistic pollen particle suspended in a laminar pipe flow. The computational setup is the same as employed in Section 3.4. In this context, we study four different shape approximations, namely spherical, prolate ellipsoidal, triaxial ellipsoidal, and superellipsoidal as well as common shape factors, see Hölzer and Sommerfeld (2008), Haider and Levenspiel (1989) and Leith (1987). The particles considered alongside the resistance tensor coefficients of the studied particles were taken from Štrákl et al. (2022a) and are repeated in Table 3 for convenience.

Table 3 shows that the higher the complexity of the particle shape, the better the agreement between the \mathbf{K}' , $\mathbf{\Omega}'$ and $\mathbf{\Pi}'$ tensor coefficients of the particle and the pollen replica, (Štrákl et al., 2022a). Consequently, the largest deviations are obtained for the spherical particle approximation and the best fit for the superellipsoidal particle. Moreover, we investigate common shape factors presented in literature, i.e. Haider and Levenspiel (1989), Leith (1987) and Hölzer and Sommerfeld (2008). These shape factors are further applied to a spherical

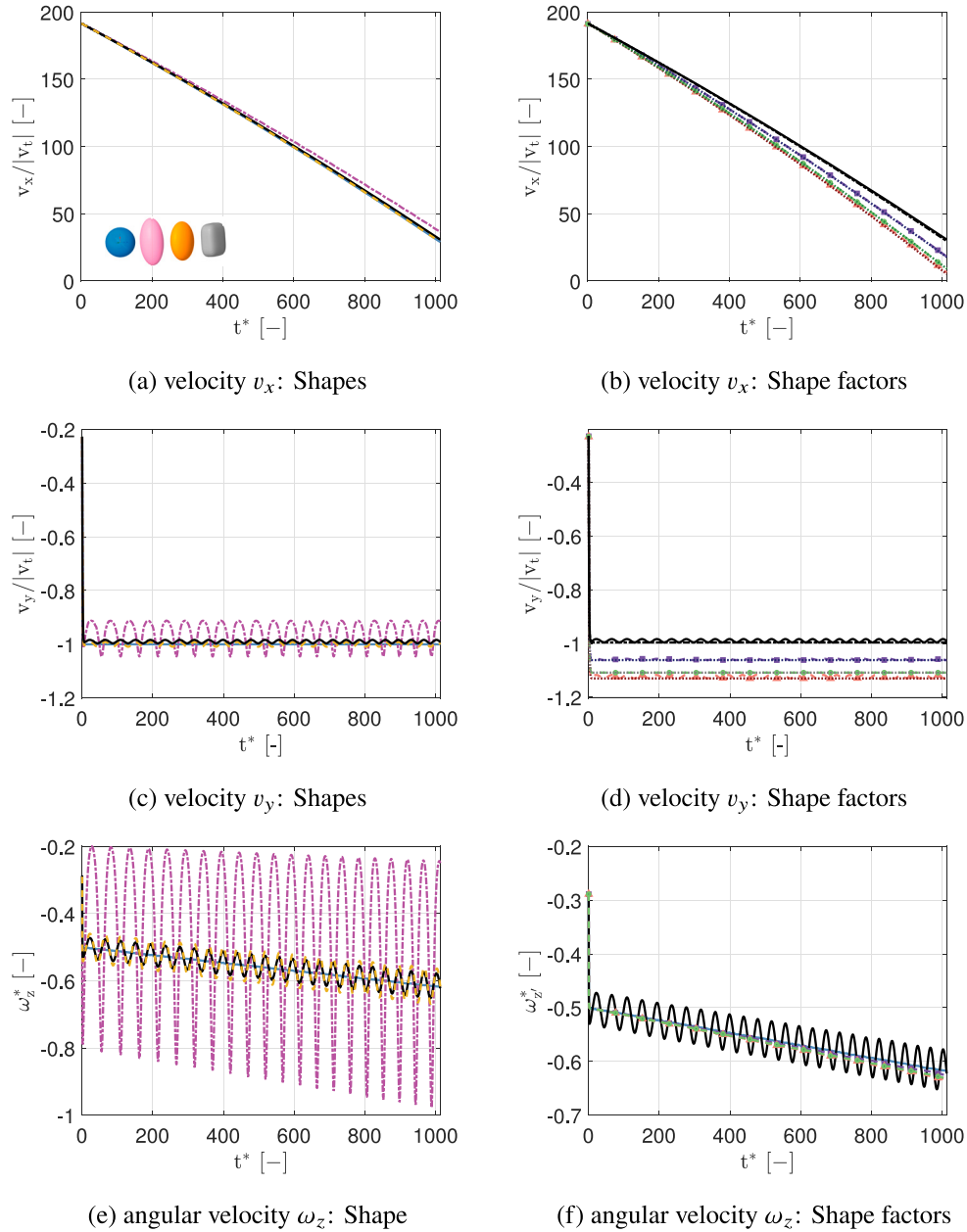


Fig. 10. Velocity v and angular velocity ω components of four different particle shapes in a laminar pipe flow. Non-dimensional parameters: $t^* = t_{Sim}/\tau_p$, $\omega_i^* = \omega_i/\omega_f$ ($i = x, y, z'$) with flow vorticity at the injection position $\omega_f = 726.95 \text{ rad/s}$. Initial orientation: $\varphi = -90^\circ$, $\theta = 0^\circ$, $\psi = 0^\circ$; ■ A, ■ B, ■ C, ■ D2, ■ D1, ■ E1, ■ F1, ■ G1, ■ E2, ■ F2, ■ G2.

shape to account for non-sphericity effects. Note, however, that as shown in Table 3, the obtained shape factors lead to a larger deviation for $K'2c/d_{eq}$ to the reference pollen particle than the spherical shape. In addition, the rotation of the spherical particles using shape factors is either neglected (E1, F1, G1) or taken into account (E2, F2, G2).

In the following, we investigate the influence of the considered particle shapes on the particle motion. In this context, we set the volume equivalent diameter d_{eq} for all considered shapes to $d_{eq} = 5 \mu\text{m}$ and the density to 2560 kg/m^3 , with a particle volume of $V_p = 65.45 \mu\text{m}^3$. Considering the domain dimensions, the non-dimensional pipe diameter is $D^* = D/d_{eq} = 840$ and the non-dimensional pipe length is $L^* = L/d_{eq} = 140000$. Note that the particles are suspended in a laminar air flow with a fluid density of $\rho_f = 1.208 \text{ kg/m}^3$ and thus $\rho_p \gg \rho_f$. The particle response times of the volume equivalent sphere is $\tau_p = 0.197 \text{ ms}$, see Eq. (11). Furthermore, using Eq. (10) we can obtain the volume equivalent particle Stokes number St , which renders $St =$

$0.046 \ll 1$ for all particle shapes considered. In addition, we evaluate the analytical terminal velocity of a settling sphere, see Eq. (13) which gives $|v_t| \approx g/\tau_p$ ($= 0.001936 \text{ m/s}$ with $g = 9.81 \text{ m/s}^2$). Followingly, the maximal descent y_{max} of the spherical particle in the considered simulation time of $t_{max} = 1013\tau_p$ ($\approx 0.2 \text{ s}$), renders $y_{max} = 77.44 d_{eq}$.

Since the superellipsoidal particle most accurately reproduces the tensor coefficients of the pollen replica (see Table 3), it will serve as a reference in the following analysis. In all cases considered, the particle is initialized with the flow velocity present at the particular injection position and zero angular velocity.

Orientation A:

First, the initial orientation of the particles under consideration is set as follows: $\varphi = -90^\circ$, $\theta = 0^\circ$, $\psi = 0^\circ$, which describes an initial perpendicular orientation of the major semi-axis of the particles to the flow direction. Fig. 9 presents the resulting directional cosines

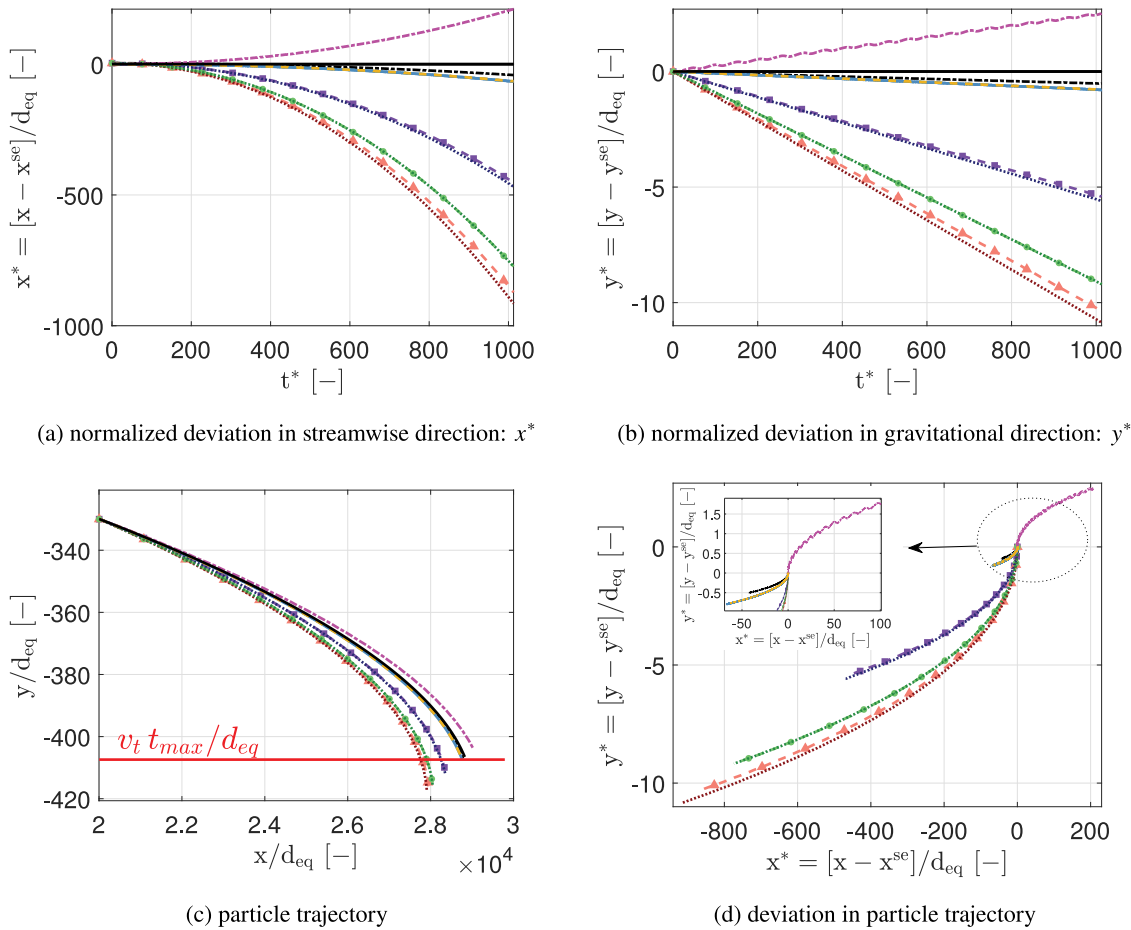


Fig. 11. Deviation of particle position compared to superellipsoid particle position (x^{se} , y^{se}). The deviation is normalized to the volume equivalent diameter of a sphere (d_{eq}). The initial particle orientation is set to $\varphi = -90^\circ$, $\theta = 0^\circ$, $\psi = 0^\circ$. $\color{cyan}\blacksquare$ A, $\color{magenta}\blacksquare$ B, $\color{yellow}\blacksquare$ C, $\color{black}\blacksquare$ D2, $\color{black}\blacksquare$ D1, $\color{green}\blacksquare$ E1, $\color{red}\blacksquare$ F1, $\color{blue}\blacksquare$ G1, $\color{green}\blacksquare$ E2, $\color{red}\blacksquare$ F2, $\color{purple}\blacksquare$ G2, $\color{red}\blacksquare$ maximal descent of a settling sphere in Stokes flow ($y_{max}/d_{eq} = v_t t_{max}/d_{eq}$).

$\cos(x)$ and $\cos(z)$. Note that for the chosen initial orientation we obtain $\cos(z) = 0$.

As displayed in Fig. 9, a good agreement of directional cosines can be obtained between the triaxial particle, the spherical particle and the superellipsoid reference geometry. However, in the case of the prolate ellipsoid, the rotational motion varies visibly. While the directional cosines in x and y for the spherical, the triaxial, and the superellipsoidal particle resemble harmonic oscillations, see Fig. 9, the prolate ellipsoid rotation is similar as presented in Section 3.4.1, see Fig. 7. The rotational motion of the prolate ellipsoid agrees well with the superellipsoidal shapes until the first flow-alignment orientation is reached ($t_{sim} \approx 22\tau_p \approx 0.0043$ s). As can be seen in Fig. 9, the prolate ellipsoidal particle traverses the flow-aligned orientation more slowly than the remaining shapes considered, resulting in a smaller number of revolutions after $t_{max} = 1013\tau_p (\approx 0.2$ s), i.e three revolutions less. Note that this extended time of traversing the flow-alignment leads to a higher average projected particle area in the gravitational direction and subsequently a smaller average projected area in streamwise direction than for the remaining shapes considered. In the following, we evaluate the evolution of the velocity v as well as the angular velocity ω of the examined particle shapes, see Fig. 10.

As shown in Fig. 10, both the velocity v_x and v_y as well as the angular velocity $\omega_{x'}$ of the studied particles differ notably. Note that the remaining velocity and angular velocity components render $v_y = 0$ and $\omega_{x'} = \omega_{y'} = 0$ for the chosen initial orientation.

While the prolate ellipsoid moves visibly faster in the flow direction, the velocity variations of the spherical, triaxial, and superellipsoidal particles are minor, see Fig. 10(a). When comparing Figs. 10(a) and

10(b), we find that for all shape factors considered, the deviations from the superellipsoid reference exceed the errors of the shape approximations used, i.e. sphere without shape factors, prolate ellipsoid, triaxial ellipsoid. Looking at the vertical velocity v_y of the prolate ellipsoidal particles, additional variations are observed, with the oscillation being strongest in v_y and the overall average descent velocity $|\bar{v}_y|$ being smallest among the particle shapes considered, see Fig. 10(c). We attribute these effects to the fact that the flow-alignment orientation of the prolate ellipsoid is traversed the slowest, as shown in Fig. 9. This leads to an increased time period in which the largest projected area is present in the direction of gravity, giving the smallest average settling velocity, and consequently the smallest projected area in the direction of flow, rendering an increased horizontal velocity v_x . Due to the flow configuration considered, the slower descent of the prolate ellipsoid leads to the effect that it experiences a higher flow velocity during its entire motion through the pipe than the remaining particles. The remaining particle shapes sink faster and thus experience a lower flow velocity as the velocity decreases in gravitational direction towards the pipe wall. As shown in Fig. 10(d), however, the shape factors again lead to the largest deviations from the superellipsoidal reference shape, which we account to the large deviations in K^2c/d_{eq} components as presented in Table 3. In addition, we study the angular velocity $\omega_{z'}$, see Fig. 10(e,f). As shown, the simulation of the considered pollen particle using a spherical (with or without shape factors) as well as prolate ellipsoidal shape approximation is not justified as the superellipsoidal angular velocity cannot be adequately reproduced. While the change in angular velocity is constant for the spherical shape, the angular velocity of the prolate ellipsoidal particle depends strongly on the orientation,

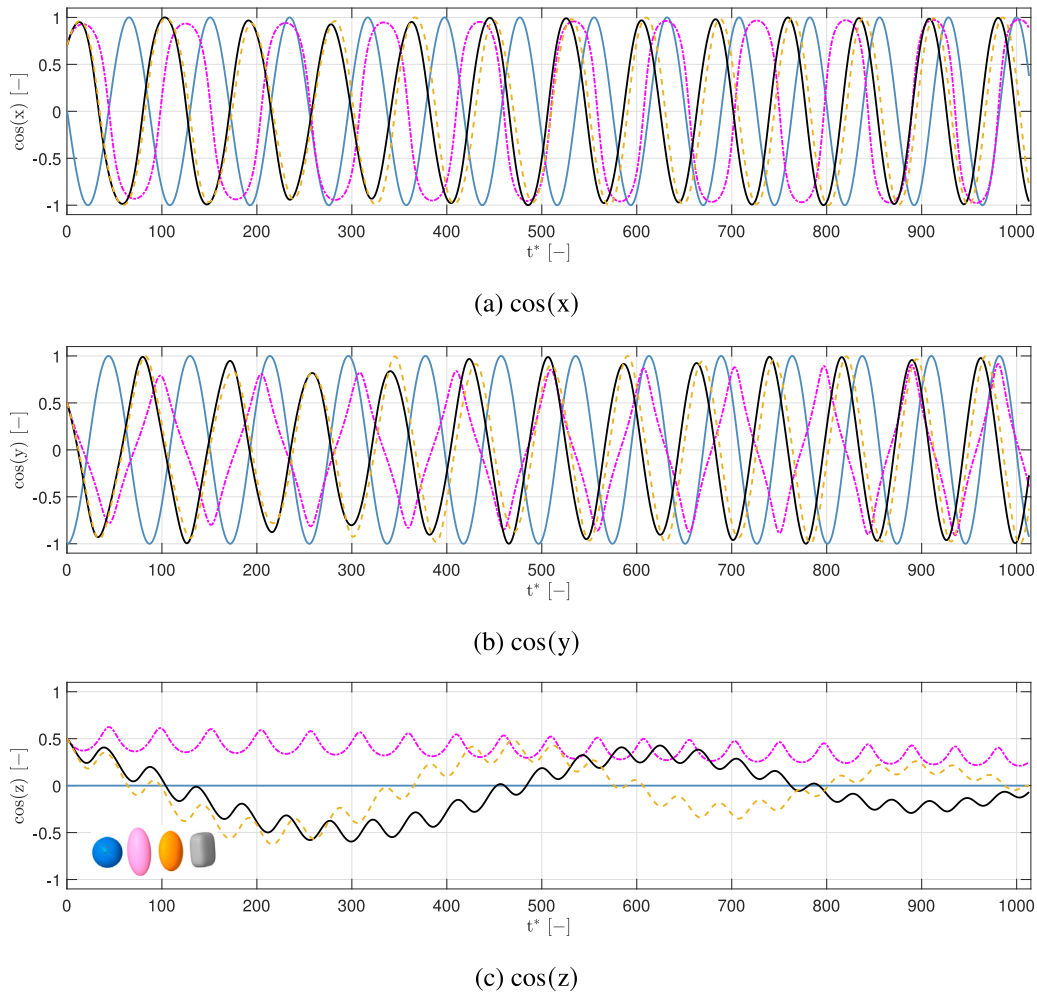


Fig. 12. Directional cosines of four different particle shapes in a laminar pipe flow. Non-dimensional parameter: $t^* = t_{sim}/\tau_p$. Initial orientation $\varphi = 0^\circ$, $\theta = 45^\circ$, $\psi = 45^\circ$; ■ A, ■ B, ■ C, ■ D2.

i.e the angular velocity is lowest when traversing the flow-aligned orientation and increases most rapidly when it is not aligned. However, the triaxial and superellipsoidal approximations still agree sufficiently.

Next, we investigate the resulting particle trajectories. Fig. 11 (a, b) evaluates the relative deviation (x^* , y^*) of the particle position (x , y) with respect to the superellipsoidal particle position (x^{se} , y^{se}). Note that the deviations are normalized to the volume equivalent diameter ($d_{eq} = 5 \mu\text{m}$) of the particles. As shown in Fig. 11, the particle position changes strongly with particle shape. After $t_{max} = 1013\tau_p$ ($\approx 0.2 \text{ s}$), the streamwise position of the prolate ellipsoid deviates from the superellipsoidal reference by more than $200 \times d_{eq}$, as a consequence of the higher v_x , while the sphere using shape factors deviates between $500 - 900 \times d_{eq}$, see Fig. 11 (a) In contrast, better agreement with the superellipsoidal horizontal position is obtained for both the spherical and triaxial shape approximations, although still with a visibly deviation of $65 \times d_{eq}$. Moreover, the prolate particle deviates more than twice as much from the superellipsoidal reference in the vertical direction as the spherical (without shape factors) and triaxial shapes, see Fig. 11 (b). Furthermore, we observe that the use of shape factors again produces the greatest deviations between $5 - 10 \times d_{eq}$ in y direction. For all shapes and shape factors considered, the deviation from the superellipsoidal reference particle is more pronounced in the flow direction than in the gravitational direction. Moreover, we include the analytic maximum descent of a settling sphere $y_{max} = v_t t_{max}$ in Stokes flow in Fig. 11 (c), see Eq. (13). As can be seen, the descent of the simulated spherical particle using the novel superellipsoidal tracking agrees excellently with the obtained analytical y -position while the shape factors lead

to an increased vertical motion. For the initial orientation chosen, the shape factors simulations with rotation lead to a comparable result to the shape factor simulations without rotation. In the case of the shape factors proposed by Leith (1987) considering rotation does not change the results, since $K'_{xx} = K'_{yy} = K'_{zz}$.

In general, it is observed that the triaxial ellipsoid for the initial orientation $\varphi = -90^\circ$, $\theta = 0^\circ$, $\psi = 0^\circ$ agrees well with the superellipsoidal motion in terms of rotation and velocity, with the main deviation occurring in the streamwise propagation. Moreover, the spherical particle differs mainly in terms of rotational motion, since a constant change of ω_z is observed, while the change of angular velocity of the considered superellipsoidal particle varies depending on its orientation to the flow. Due to the extended traversing time of the flow alignment orientation, the prolate ellipsoidal shape is not able to reproduce the general motion of the superellipsoidal particle under consideration. Furthermore, the shape factors both with and without rotation lead to a strongly differing particle motion and produce higher deviations than the sphere without shape factors.

Orientation B:

In the next step, the initial orientation is set as follows: $\varphi = 0^\circ$, $\theta = 45^\circ$, $\psi = 45^\circ$. By changing the initial orientation, a rotational motion about all particle semi-axes is observed, as shown in Fig. 12.

In agreement with the previously used orientation (Orientation A), Fig. 12 shows that the prolate ellipsoid exhibits the highest errors in reproducing the direction cosines of the superellipsoidal reference, as it experiences a longer transit time through the flow-aligned orientation.

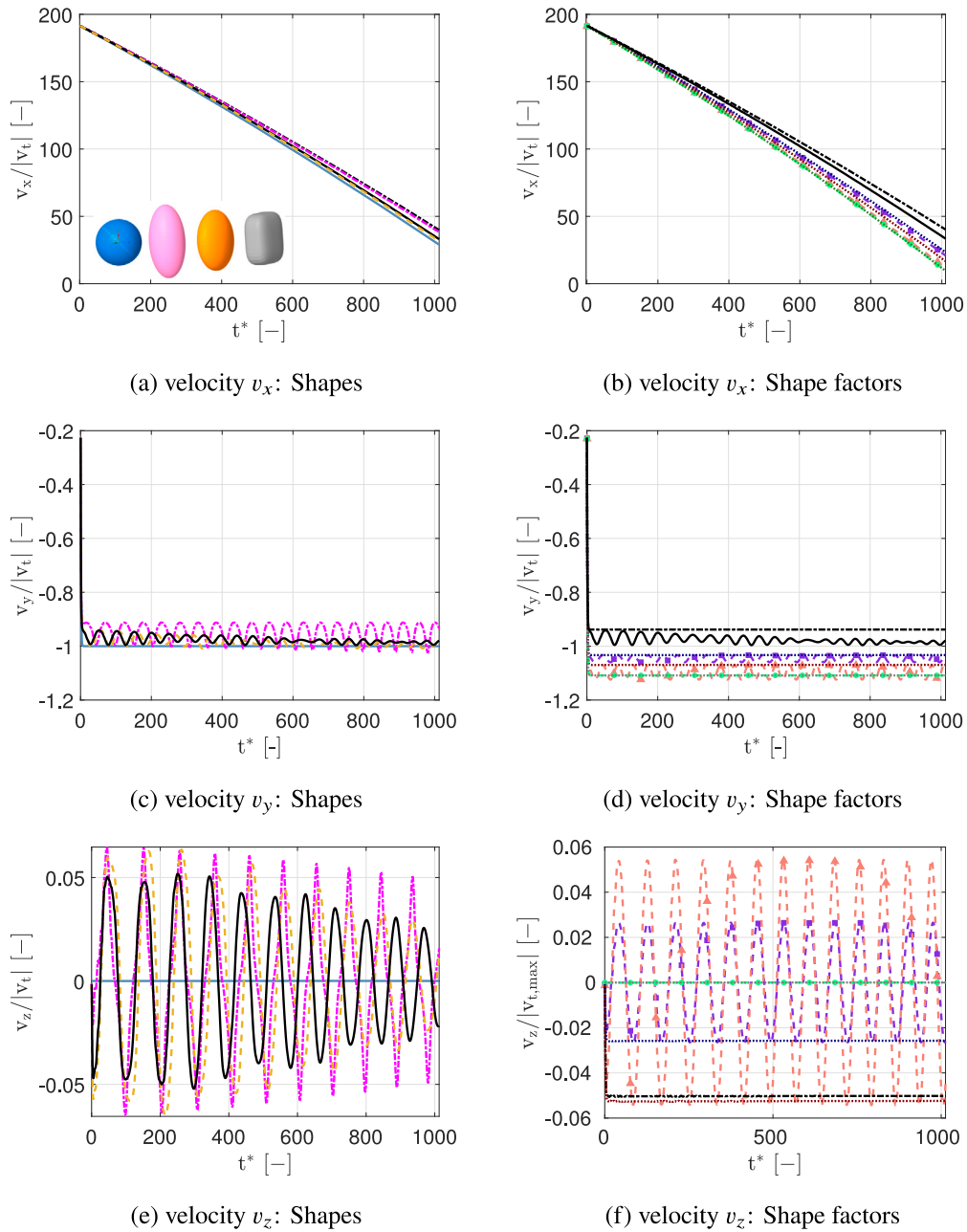


Fig. 13. Velocity v components of four different particle shapes. Non-dimensional parameters: $t^* = t_{Sim}/\tau_p$. Initial orientation $\varphi = 0^\circ$, $\theta = 45^\circ$, $\psi = 45^\circ$: ■ A, ■ B, ■ C, ■ D2, ■ D1, ■ E1, ■ F1, ■ G1, ■ E2, ■ F2, ■ G2.

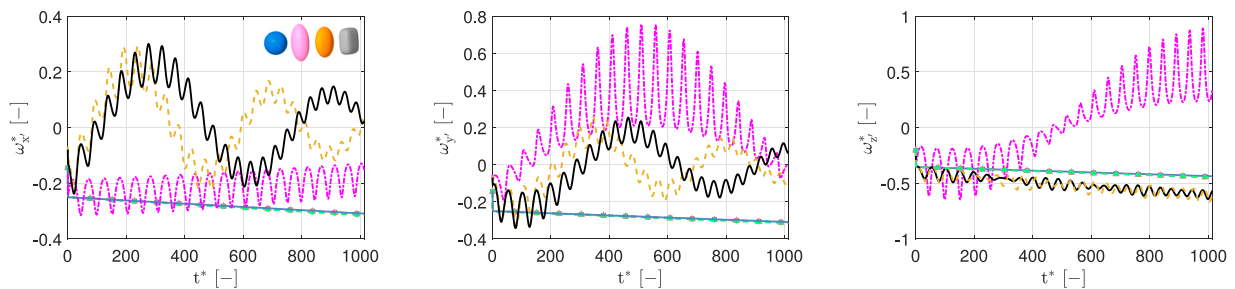


Fig. 14. Angular velocity ω components of four different particle shapes. Non-dimensional parameters: $t^* = t_{Sim}/\tau_p$, $\omega_i^* = \omega_i/\omega_f$ ($i = x', y', z'$) with flow vorticity at the injection position $\omega_f = 726.95$ rad/s. Initial orientation $\varphi = 0^\circ$, $\theta = 45^\circ$, $\psi = 45^\circ$: ■ A, ■ B, ■ C, ■ D2, ■ E2, ■ F2, ■ G2.

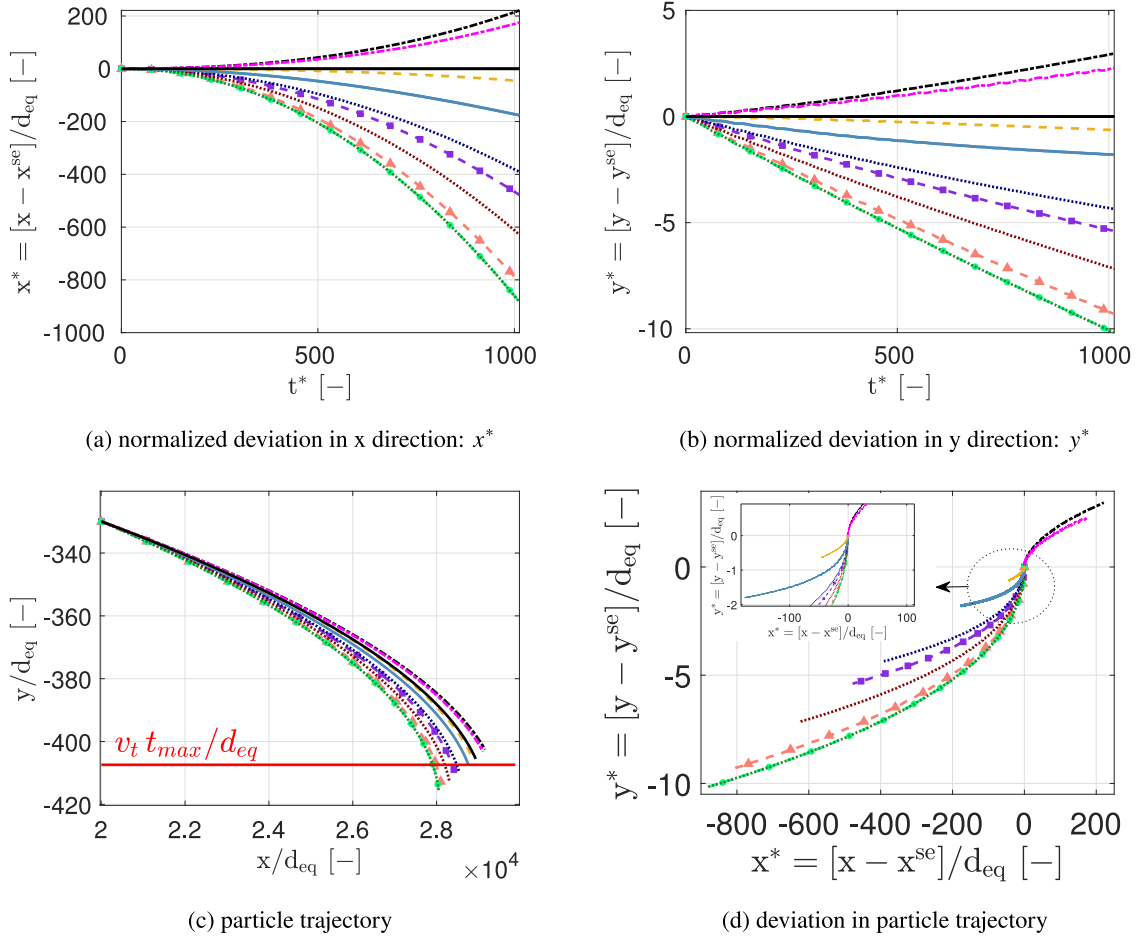


Fig. 15. Deviation of particle position compared to superellipsoid particle position (x^{se} , y^{se}). The deviation is normalized to the volume equivalent diameter of a sphere (d_{eq}). The initial particle orientation is set to $\varphi = 0^\circ$, $\theta = 45^\circ$, $\psi = 45^\circ$. — A, — B, — C, — D2, — D1, — E1, — F1, — G1, — E2, — F2, — G2, — maximal descent of a settling sphere in Stokes flow ($y_{max}/d_{eq} = v_t t_{max}/d_{eq}$).

In addition, deviations from the directional cosines of the superellipsoidal reference particle are visible when a spherical or triaxial shape approximation is used. Overall, the triaxial particle achieves the best fit to the rotational motion of the superellipsoidal particle. Nevertheless, Fig. 12 indicates that using a simplified shape such as sphere, prolate ellipsoid, or triaxial ellipsoid is not sufficient to accurately reproduce the rotational motion of the superellipsoidal reference.

Furthermore, we investigate the velocities and angular velocities of the differently shaped particles considering the changed initial orientation. A similar trend is observed in the resulting velocity as for the initial orientation used previously (Orientation A), with the velocity in the flow direction being lowest for the spherical shape with shape factors and highest for the prolate ellipsoid, see Fig. 13 (a, b). Moreover, as shown in Fig. 13 (c,d), $|v_y|$ is highest for the spherical particle using shape factors, while the prolate ellipsoid falls the slowest among the particle shape approximations used. Note that applying shape factors to the spherical particle again leads to higher deviations, both in the rotating and non-rotating cases, see Fig. 13 (b,d).

In addition, Fig. 14 present a strong influence of the particle shape on the resulting angular velocity. While the prolate ellipsoidal shape and the spherical particle (both with and without shape factors) give strong deviations from the superellipsoidal motion, the triaxial particle results in the best agreement, nevertheless, with clearly visible differences.

In a final step, we evaluate the resulting particle trajectories. As shown in Fig. 15, the particle position varies strongly between the particle shapes considered. After $t_{max} = 1013\tau_p$, the streamwise motion of the prolate ellipsoidal and the spherical particle deviate from the

superellipsoidal reference by more than $175 \times d_{eq}$ and $-176 \times d_{eq}$, respectively. In contrast, better agreement with the superellipsoidal motion in flow direction is obtained for the triaxial shape approximation, however, still with notably less progression in the x direction. Moreover, the prolate and spherical particle deviate more than twice as much from the superellipsoidal reference in the vertical direction as the triaxial shape, see Fig. 15 (b). In addition, we observe that employing shape factors again leads to a stronger deviation than using a sphere without shape factors. Besides, for all particles studied, the deviation from the superellipsoidal reference is more pronounced in the streamwise than in the gravitational direction. In summary, this test case underlines the importance of an accurate shape approximation, as even the best-fitted sphere, prolate ellipsoid, and triaxial ellipsoid of the pollen replica resulted in significantly altered particle motion.

Superellipsoid Particle Clouds:

In a third test case, we inject 10^5 particles over 80% of the pipe diameter to analyze the motion of particle clouds composed of different particle shapes. The initial position and orientation of the particles are random and the particles are initialized with the flow velocity at the injection position. The properties of the particle clouds are obtained by averaging over the number of injected particles ($n = 10^5$). For example, the centroid in the streamwise direction is determined as follows (all other cloud properties are determined analogously):

$$\bar{x} = \frac{\sum_{i=1}^n x_i}{n}, \quad (41)$$

where x_i denotes the x-coordinates for particle i with $i = 1 \dots n$ and n labeling the number of particles per particle cloud. As presented in

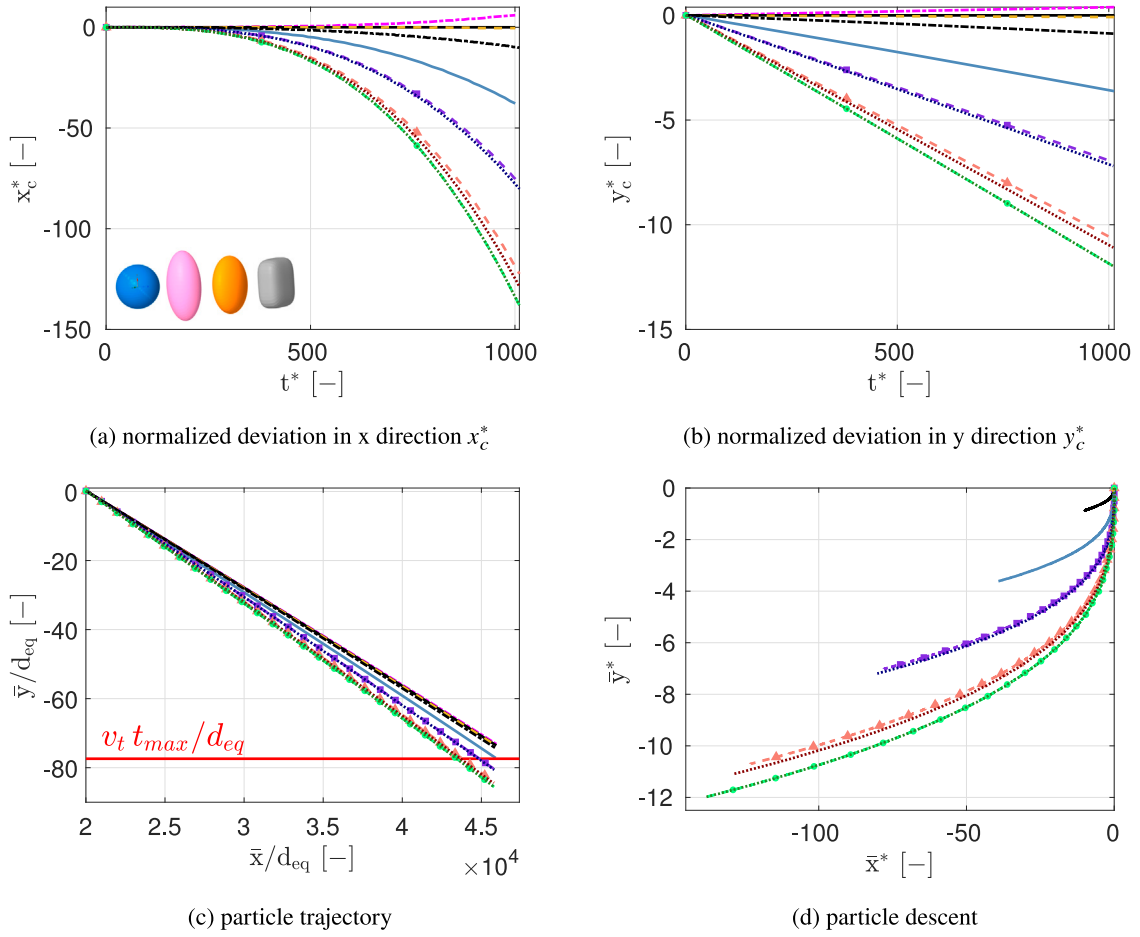


Fig. 16. Normalized deviation of particle cloud position \bar{x} and \bar{y} compared to superellipsoid particle cloud position $(\bar{x}^{se}, \bar{y}^{se})$. The deviation is normalized to the volume equivalent diameter of a sphere (d_{eq}): $x_c^* = [\bar{x} - \bar{x}^{se}]/d_{eq}$ (analogously for y_c^*). The particles are injected with random orientation. ■ A, ■ B, ■ C, ■ D2, ■ D1, ■ E1, ■ F1, ■ G1, ■ E2, ■ F2, ■ G2, ■ maximal descent of a settling sphere in Stokes flow ($y_{max}/d_{eq} = v_t t_{max}/d_{eq}$).

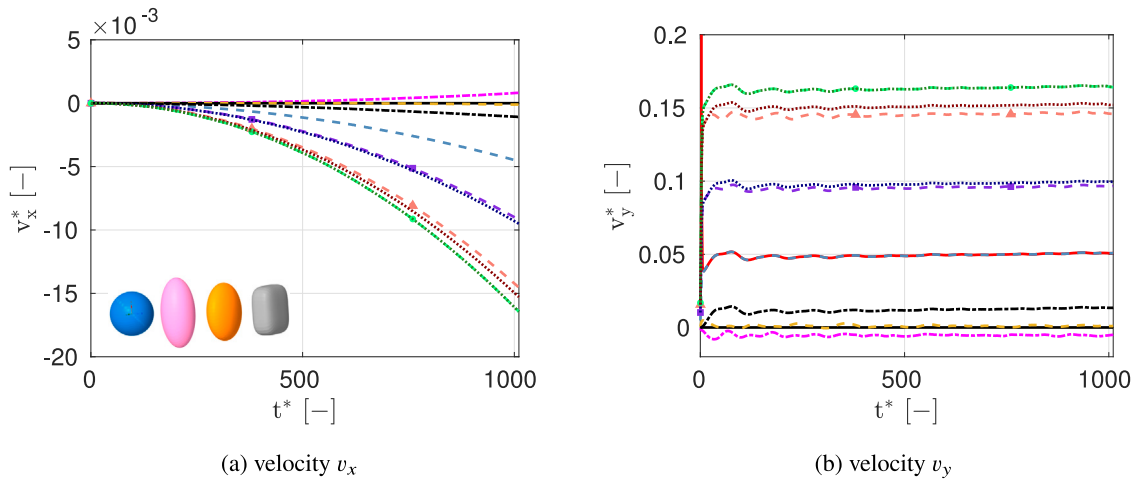


Fig. 17. Normalized deviation of particle cloud velocity components \bar{v}_x and \bar{v}_y compared to superellipsoid particle cloud velocity: $v_x^* = [\bar{v}_x - \bar{v}_x^{se}]/\bar{v}_x^{se}$ (analogously for \bar{v}_y^*). The particles are injected with random orientation. ■ A, ■ B, ■ C, ■ D2, ■ D1, ■ E1, ■ F1, ■ G1, ■ E2, ■ F2, ■ G2, ■ G2, ■ maximal descent of a settling sphere in Stokes flow ($[v_t t_{max} - \bar{v}_y^{se}]/\bar{v}_y^{se}$).

Fig. 16 (a, b), the deviations in the streamwise direction (x -coordinate) are more pronounced than the deviations in the gravitational direction (y -coordinate) for all particle clouds considered. Moreover, a spherical particle approximation leads to the strongest errors in predicting the superellipsoid cloud center in both x and y directions. After $t_{max} = 1013\tau_p$, the spherical cloud center (without shape factors) falls behind

the superellipsoidal cloud by more than $35 \times d_{eq}$ in the flow direction, while in the gravity direction the cloud center descends by more than $3 \times d_{eq}$. Note that using the presented shape factors (Leith, 1987; Haider and Levenspiel, 1989; Hölzer and Sommerfeld, 2008) increases the deviation to more than $75 \times d_{eq}$ and $6 \times d_{eq}$ in x and y direction, respectively. **Fig. 16** presents that even a simplification using prolate

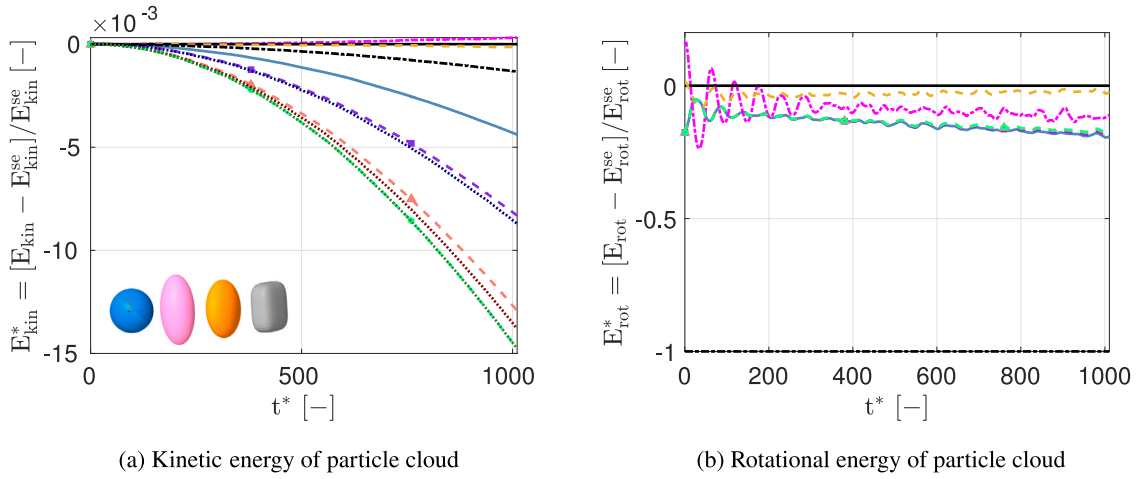


Fig. 18. Normalized deviation of particle cloud kinetic and rotational energy compared to superellipsoid particle cloud kinetic and rotational energy: $E_{rot}^* = [\bar{E}_{rot} - \bar{E}_{rot}^{se}] / \bar{E}_{rot}^{se}$ (analogously for E_{kin}^*). The particles are injected with random orientation. — A, — B, — C, — D2, — D1, — E1, — F1, — G1, — E2, — F2, — G2.

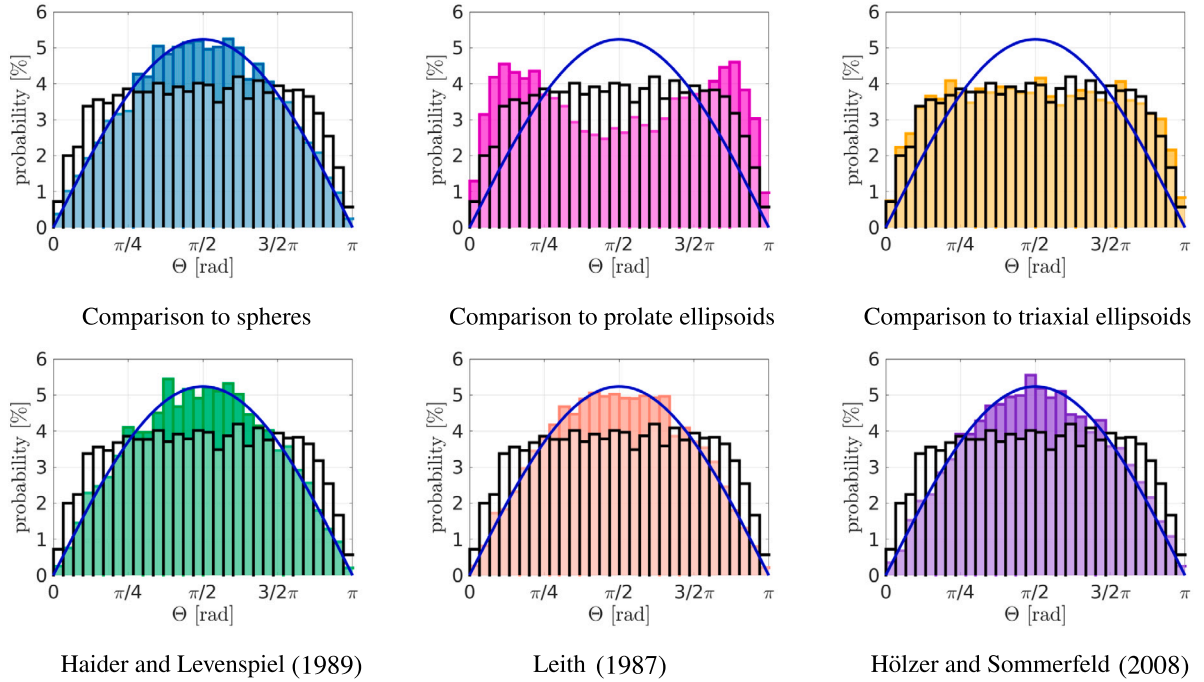


Fig. 19. Probability function of particle long axis orientation in pipe flow at $t_{max} = 1013\tau_p$, — initial distribution of particle long axis orientations, — A, — B, — C, — D2, — E2, — F2, — G2.

ellipsoidal particles leads to visible differences in the prediction of the cloud center, however, these differences are much smaller than those obtained by assuming a cloud consisting of spherical particles (with or without shape factors). On the contrary, the particle cloud consisting of triaxial ellipsoids is able to replicate the horizontal and vertical motion of the superellipsoidal reference with sufficient accuracy, since the deviations are minor in both x and y directions. We also determine the maximum vertical velocity of a sphere settling in Stokes flow, see Eq. (13), which is shown in Fig. 16(c). It can be seen that excellent agreement is obtained between the vertical movement of the spherical cloud obtained with the novel superellipsoid particle tracking and the analytical results for a spherical particle settling in Stokes flow. Note that after $t_{max} = 1013\tau_p$ all the studied shapes, i.e. spherical, prolate ellipsoidal, triaxial ellipsoidal, and superellipsoidal, lead to overall smaller deviations of the cloud trajectories compared to the spherical particle cloud using shape factors, see Fig. 16(d).

Next, we examine the resulting velocities of the particle clouds, as shown in Fig. 17(a, b). As can be seen in Fig. 17(a), we observe the largest deviations in the flow direction for the spherical shape and the smallest differences for using the triaxial ellipsoid approximation. A similar trend is also observed in the gravitational direction, Fig. 17(b). In addition, Fig. 17(b) contains the analytically determined terminal velocity of a sphere in Stokes flow, see Eq. (13), which is again in excellent agreement with the numerically obtained spherical cloud motion (without shape factors).

In addition, the relative deviation of particle kinetic and rotational energy is investigated. As can be seen in Fig. 18, there are visible deviations in kinetic and rotational energy for the particle clouds studied. Considering the superellipsoidal particle cloud as a reference, the triaxial approach achieves the best agreement in both kinetic and rotational energy, while the spherical particle cloud differs the most. Note that the deviation in rotational energy is significantly larger than in kinetic energy for all shapes considered. The shortcomings of

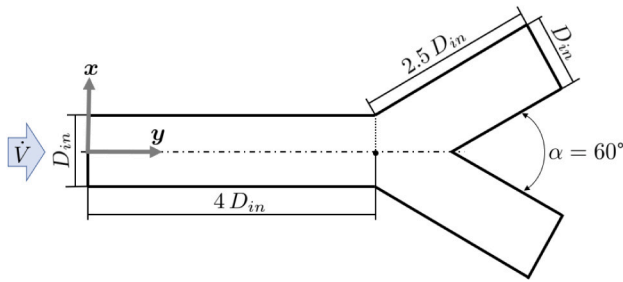


Fig. 20. Sketch of the simplified bifurcation model. Gravitational direction: y .

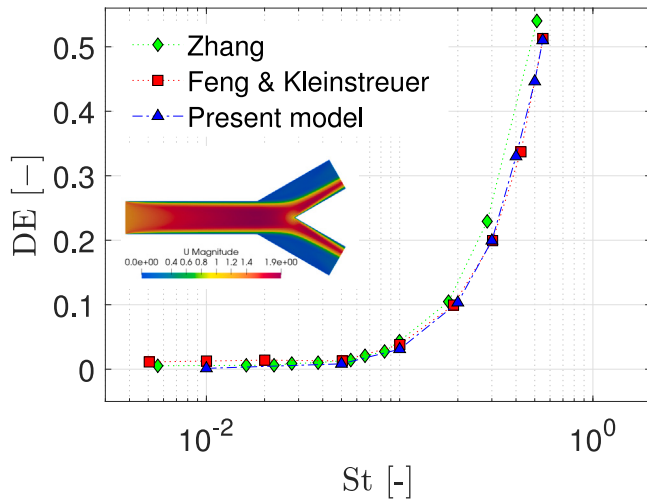


Fig. 21. Deposition efficiency $DE [-]$ in a simplified bifurcation for prolate ellipsoid with $\lambda = 20$. DE denotes ratio of deposited particles to injected particles.

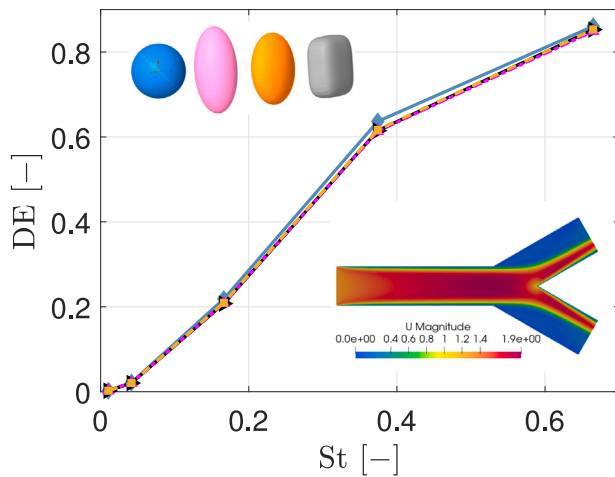


Fig. 22. Deposition efficiency $DE [-]$ in a simplified bifurcation for sphere, prolate ellipsoid, triaxial ellipsoid and superellipsoid approximation of the pollen replica presented in Section 3.4.2. DE denotes ratio of deposited particles to injected particles. $\color{cyan}\blacktriangle$ A, $\color{magenta}\blacksquare$ B, $\color{orange}\blacklozenge$ C, $\color{black}\bullet$ D2.

both the spherical and prolate ellipsoidal shape approximations are apparent, as the errors in the rotational energy reach up to $\bar{E}_{rot}^* = 20\%$ for the sphere without shape factors and $\bar{E}_{rot}^* = 10\%$ for the ellipsoid particle cloud. Consequently, the rotational energy of the superellipsoidal particle cloud cannot be sufficiently reproduced by either spherical or prolate ellipsoidal particles.

In addition, Fig. 19 displays the probability of particle orientation at $t_{max} = 1013\tau_p$. For this purpose, we evaluate the angle between the long axis a of each particle and the streamwise flow direction. In Fig. 19 we

have included the initial particle orientation at the time of injection and the results of the superellipsoidal particle cloud for reference. Fig. 19 clearly shows the importance of an accurate shape approximation for reliable statistical data on particle orientation, since the resulting distribution of particle orientation strongly depends on the chosen approximation shape. As shown, there is no preferred orientation for the superellipsoidal particles, while we observe a preferred orientation for the prolate ellipsoidal particles, which tend to align with the flow direction. We also find that the orientation of the spherical particles resembles the initial injection distribution. In addition, we find that the application of shape factors to rotating spheres does not significantly change the obtained rotational distribution at $t_{max} = 1013\tau_p$.

3.5. Bifurcation

The final validation case refers to a simplified 3D bifurcating airway. The diameters of the parent and daughter airways are $D_{in} = 6$ mm, based on the third generation of Weibel's symmetric lung model, (Weibel, 1963), and are consistent with the setup employed by Feng and Kleinstreuer (2013). For a sketch of the computational domain, see Fig. 20.

The selected airway model has a bifurcation angle of $\alpha = 60^\circ$ according to Zhang et al. (1996) and Feng and Kleinstreuer (2013). Note that no information on the radius at the separation into two tubes is given. The Reynolds number considered is $Re = 500$ to mimic normal breathing conditions in the third generation, (Zhang et al., 1996). In this validation, we analyze the deposition efficiency for different Stokes numbers St by considering prolate particles with aspect ratio $\lambda = 20$ and particle density $\rho_p = 2400$ kg/m³, see Zhang et al. (1996). In agreement with Feng and Kleinstreuer (2013), we assume a uniform inlet velocity and release 10^5 randomly distributed fibers. Moreover, the elongated prolate spheroids are injected with a random orientation and an initial velocity of zero at the parent inlet site. In this study, deposition is assumed to occur when particle-wall contact is established, thus deposition by impaction as well as interception (particle comes close enough to a wall that a particle edge touches the wall surface) are included, see Section 2.3. It is an important mechanism for elongated particles such as fibers for which the ratio between length and diameter is large. Fibers are assumed to escape the geometry if they dwell in the bifurcation model ten times longer than the average residence time of the flow, see Zhang et al. (1996). For convenience, Table 4 summarizes the computational details of the particle tracking.

To validate the developed wall interaction model for superellipsoids, we draw on the numerical results of Zhang et al. (2015) and Feng and Kleinstreuer (2013) as references. As shown in Fig. 21, there is excellent agreement of the deposition efficiency with the numerical results of Feng and Kleinstreuer (2013) for all particle Stokes numbers studied, with the deposition being slightly reduced for particle Stokes numbers of order $St = 10^{-2}$. Consequently, we consider the novel superellipsoidal deposition model (described in Section 2.3) as validated.

Furthermore, we apply the novel superellipsoid particle tracking including the validated superellipsoid deposition model to study the deposition efficiency within the bifurcation used for the different particle shapes described in Section 3.4.2. As shown in Fig. 22, a good agreement is obtained between the deposition efficiency for prolate and triaxial ellipsoids as well as for superellipsoids in the studied range of particle Stokes numbers. In the case of the spherical particle cloud, slight deviations are visible in the intermediate range of the particle Stokes numbers examined.

In a next step, we compare the position statistics in streamwise (x) and in gravitational direction (y) for the particle clouds with $d_{eq} = 15$ μm ($St \approx 0.38$). The obtained position probabilities are shown in Fig. 23. As displayed, the overall distribution of the considered particle shapes is almost identical. However, there are slight deviations in the distribution of the prolate ellipsoids, since the deposition of

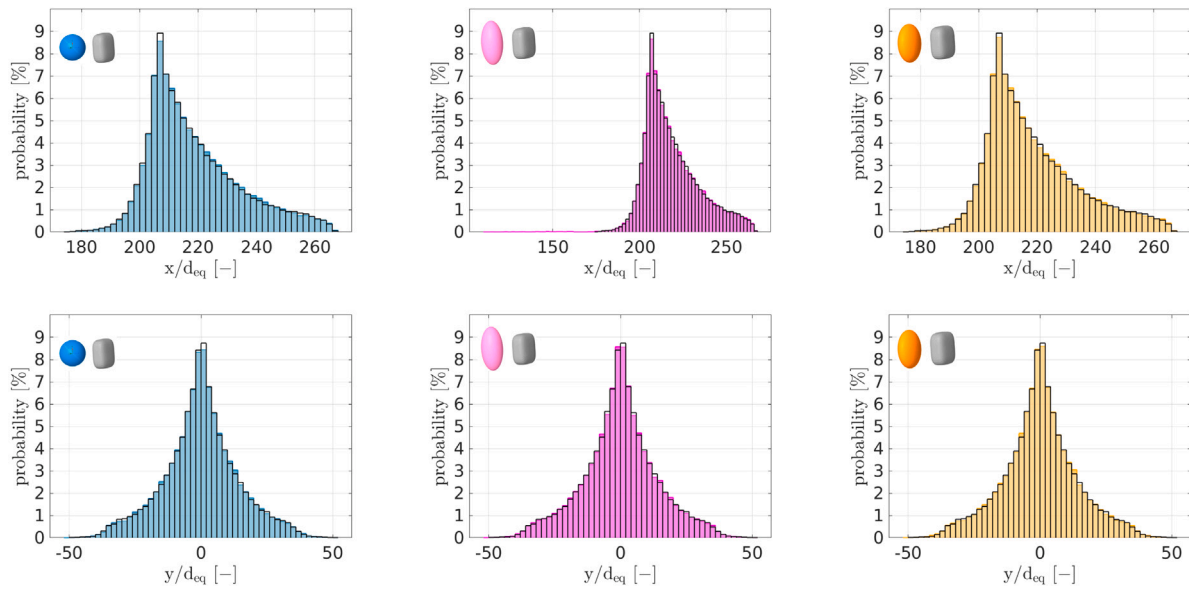


Fig. 23. x/d_{eq} and y/d_{eq} (y : gravitational direction) deposition probability in a simplified bifurcation for sphere, prolate ellipsoid, triaxial ellipsoid and superellipsoid approximation of the pollen replica with $d_{eq} = 15 \mu\text{m}$, see Section 3.4.2 ■ A, ■ B, ■ C, ■ D2.

Table 4

Computational details of particle tracking.

t Integration scheme	Forces	Wall interaction	n particles	$\varphi_0, \theta_0, \psi_0$	v_0, ω_0
Implicit Euler	Drag & Gravity	Impaction & Interception ^a	10^5	Random	(0 0 0)

^aParticle comes close enough to a wall that a particle edge touches the wall surface.

the particles already occurs at lower x/d_{eq} due to a more pronounced interception effect.

Furthermore, we evaluate the deposition angle of the considered particle shapes, i.e the angle between the wall normal and particle long axis a . The obtained deposition probabilities are presented in Fig. 24. As indicated, the particle shape can affect the deposition angle on the bifurcation wall. In particular, the prolate ellipsoidal shape develops a preferred deposition angle at $\theta = \pi/2$. In contrast, the variations between spherical, triaxial, and superellipsoidal deposition orientations are negligible and remain statistically distributed.

4. Conclusions

In this study, we present force and torque models for superellipsoidal particle shapes based on the superellipsoid surrogate approach presented by Štrákl et al. (2022a,b) for simulating the motion of particles with superellipsoidal shape, developed in OpenFoam[®] and based on Lagrangian particle tracking in RANS-resolved turbulent flow. The main objective of the present study is to evaluate the trajectory and rotational motion of superellipsoidal particles in comparison with spheres (with and without shape factors) as well as prolate and triaxial ellipsoids. The main achievement of the present work is the implementation and validation of a general superellipsoid particle tracking including a wall deposition model, which can be used in CFD to approximate the dynamics and deposition (inertial impaction and interception) of more complex shaped particles. To prove the accuracy and reliability of the generated model for Lagrangian tracking of superellipsoidal particles, numerical and experimental validations were performed, i.e. a lid-driven cavity flow, a pipe flow, and a simplified bifurcation case.

First, the superellipsoid particle tracking was validated with numerical models for spheres (Tsornig et al., 2008) and prolate ellipsoids (Cui et al., 2018b) in a lid-driven cavity flow, showing excellent agreement of the results under the examined Stokes flow conditions. As a second test case, the results of the superellipsoid particle tracking were compared with numerical studies of prolate spheroids transported in

a pipe flow (Tian et al., 2012; Cui et al., 2018b). Herein, we investigated the accuracy of our superellipsoid surrogate approach presented in Štrákl et al. (2022a) compared to the reference analytical model of prolate ellipsoids. To this end, mainly negligible deviations were observed, however, in the case of strongly elongated particles, e.g. $\lambda = 14$, the rotational motion deviated slightly even for small errors in the novel superellipsoid surrogate approach proposed by Štrákl et al. (2022a). Third, a realistic pollen particle was approximated with different shapes, i.e. sphere (with or without shape factors), prolate ellipsoid, triaxial ellipsoid, and superellipsoidal shape. The tensor coefficients of the pollen replica were most accurately reproduced by the superellipsoidal shape and least accurately by the spherical shape including shape factors. We observed that when modeling complex particles, such as the pollen particle considered, simple shape approximations such as spheres or ellipsoids cannot accurately reproduce the motion, especially rotational motion, of the superellipsoidal reference particle. Besides, better agreement with the reference particle (superellipsoid) is achieved with increasing complexity of the particle shape as for example the triaxial ellipsoid. However, considering the motions of the particle clouds, the deviations between the studied shapes are small after the considered simulation time. Nevertheless, the obtained results highlight the importance of the presented novel superellipsoidal approach for improved orientation prediction for realistic (non-spherical) particles. In addition, we proposed a novel superellipsoidal wall collision model. This model was applied to a simple bifurcation and showed good agreement with results from the literature, see Zhang et al. (2015) and Feng and Kleinstreuer (2013). Future work will focus on numerical tracking of micro-sized superellipsoidal particles moving in more complex geometries, e.g. human lung replicas. For more complex shaped particles, the translation, rotation and deformation resistance tensor cannot be determined with the surrogate model of Štrákl et al. (2022a) and all tensor components have to be determined individually.

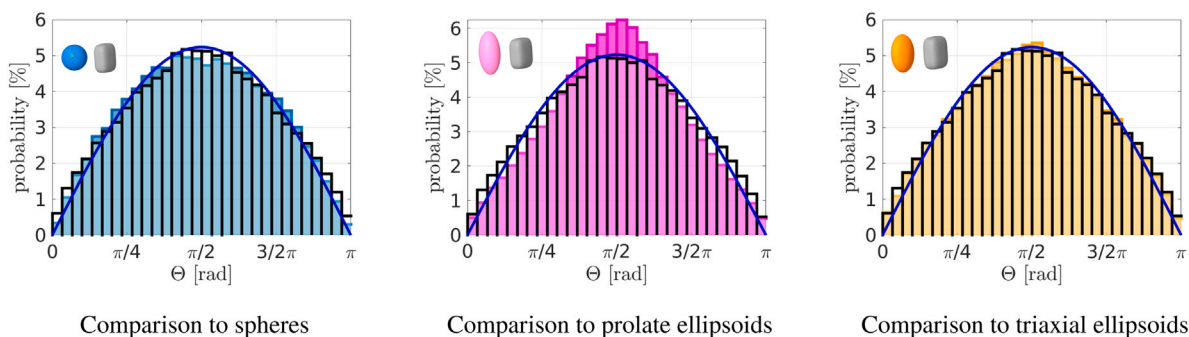


Fig. 24. Probability function of particle deposition orientation in simple bifurcation model for $d_{eq} = 15 \mu\text{m}$. ■ initial distribution of particle orientations, ■ A, ■ B, ■ C, ■ D2.

CRediT authorship contribution statement

Jana Wedel: Software, Validation, Investigation, Visualization, Writing – original draft, Conceptualization, Methodology. **Paul Steinmann:** Supervision, Reviewing and editing, Conceptualization, Project administration, Methodology, Funding acquisition. **Mitja Štrakl:** Reviewing and editing, Methodology. **Matjaž Hriberšek:** Supervision, Reviewing and editing, Conceptualization, Methodology. **Jure Ravnik:** Supervision, Reviewing and editing, Conceptualization, Methodology.

Declaration of competing interest

The authors declare that they have no known competing financial interests or personal relationships that could have appeared to influence the work reported in this paper.

Data availability

Data will be made available on request.

Acknowledgments

The authors thank the Deutsche Forschungsgemeinschaft, Germany for the financial support in the framework of the project STE 544/58-2 and the Slovenian Research Agency (research core funding No. P2-0196).

References

- Arcen, B., Ouchene, R., Khalij, M., Tanière, A., 2017. Prolate spheroidal particles' behavior in a vertical wall-bounded turbulent flow. *Phys. Fluids* 29 (9), 093301. <http://dx.doi.org/10.1063/1.4994664>.
- Bagheri, G., Bonadonna, C., 2016. On the drag of freely falling non-spherical particles. *Powder Technol.* 301, 526–544. <http://dx.doi.org/10.1016/j.powtec.2016.06.015>, URL <https://www.sciencedirect.com/science/article/pii/S0032591016303539>.
- Balachandar, S., Zaleski, S., Soldati, A., Ahmadi, G., Bourouiba, L., 2020. Host-to-host airborne transmission as a multiphase flow problem for science-based social distance guidelines. *Int. J. Multiph. Flow.* 132, 103439. <http://dx.doi.org/10.1016/j.ijmultiphaseflow.2020.103439>.
- Barr, A.H., 1981. Superquadrics and angle-preserving transformations. *IEEE Comput. Graph. Appl.* 1 (1), 11–23.
- Belka, M., Lizal, F., Jedelsky, J., Elcner, J., Hopke, P., Jicha, M., 2017. Deposition of glass fibers in a physically realistic replica of the human respiratory tract. *J. Aerosol Sci.* 117, <http://dx.doi.org/10.1016/j.jaerosci.2017.11.006>.
- Belka, M., Lizal, F., Jedelsky, J., Starha, P., Druckmullerova, H., Hopke, P.K., Jicha, M., 2016. Application of image analysis method to detection and counting of glass fibers from filter samples. *Aerosol Sci. Technol.* 50 (4), 353–362. <http://dx.doi.org/10.1080/02786826.2016.1151858>.
- Brenner, H., 1964a. The Stokes resistance of an arbitrary particle-III. Shear fields. *Chem. Eng. Sci.* 19 (9), 631–651. [http://dx.doi.org/10.1016/0009-2509\(64\)85052-1](http://dx.doi.org/10.1016/0009-2509(64)85052-1).
- Brenner, H., 1964b. The Stokes resistance of an arbitrary particle-IV arbitrary fields of flow. *Chem. Eng. Sci.* 19 (10), 703–727. [http://dx.doi.org/10.1016/0009-2509\(64\)85084-3](http://dx.doi.org/10.1016/0009-2509(64)85084-3).
- Challabotla, N.R., Zhao, L., Andersson, H., 2016. Gravity effects on fiber dynamics in wall turbulence. *Flow Turbul. Combust.* 97, <http://dx.doi.org/10.1007/s10494-016-9742-5>.
- Chiang, T., Sheu, W., 1997. Numerical prediction of eddy structure in a shear-driven cavity. *Comput. Mech.* 20, 379–396. <http://dx.doi.org/10.1007/s004660050259>.
- Cui, Z., Huang, W.-X., Xu, C.-X., Andersson, H.I., Zhao, L., 2021. Alignment of slender fibers and thin disks induced by coherent structures of wall turbulence. *Int. J. Multiph. Flow.* 145, 103837. <http://dx.doi.org/10.1016/j.ijmultiphaseflow.2021.103837>, URL <https://www.sciencedirect.com/science/article/pii/S03019322211002640>.
- Cui, Y., Ravnik, J., Hriberšek, M., Steinmann, P., 2018a. A novel model for the lift force acting on a prolate spheroidal particle in an arbitrary non-uniform flow. Part I. Lift force due to the streamwise flow shear. *Int. J. Multiph. Flow.* 104, 103–112.
- Cui, Y., Ravnik, J., Hriberšek, M., Steinmann, P., 2018b. On constitutive models for the momentum transfer to particles in fluid-dominated two-phase flows. *Adv. Struct. Mater.* 80, 1–25.
- Cui, Y., Ravnik, J., Steinmann, P., Hriberšek, M., 2019a. Settling characteristics of nonspherical porous sludge flocs with nonhomogeneous mass distribution. *Water Res.* 185, 159–170.
- Cui, Y., Ravnik, J., Verhnjak, O., Hriberšek, M., Steinmann, P., 2019b. A novel model for the lift force acting on a prolate spheroidal particle in an arbitrary non-uniform flow. Part II. Lift force taking into account the non-streamwise flow shear. *Int. J. Multiph. Flow.* 111, 232–240.
- Dastan, A., Abouali, O., Ahmadi, G., 2014. CFD simulation of total and regional fiber deposition in human nasal cavities. *J. Aerosol Sci.* 69, 132–149. <http://dx.doi.org/10.1016/j.jaerosci.2013.12.008>, URL <https://www.sciencedirect.com/science/article/pii/S0021850213002541>.
- Feng, Y., Kleinstreuer, C., 2013. Analysis of non-spherical particle transport in complex internal shear flows. *Phys. Fluids* 25, 1904. <http://dx.doi.org/10.1063/1.4821812>.
- Fennelly, K.P., 2020. Particle sizes of infectious aerosols: Implications for infection control. *Lancet Respir. Med.* 8 (9), 914–924.
- Ferziger, J.H., Perić, M., 2008. *Numerische Strömungsmechanik*. Springer, Berlin Heidelberg.
- Gallily, I., Cohen, A.-H., 1979. On the orderly nature of the motion of nonspherical aerosol particles II. Inertial collision between a spherical large droplet and axially symmetrical elongated particle. *J. Colloid Interface Sci.* 68, 338–356.
- Gallily, I., Eisner, A.D., 1979. On the orderly nature of the motion of nonspherical aerosol particles. I. Deposition from a laminar flow. *J. Colloid Interface Sci.* 68 (2), 320–337. [http://dx.doi.org/10.1016/0021-9797\(79\)90286-8](http://dx.doi.org/10.1016/0021-9797(79)90286-8), URL <https://www.sciencedirect.com/science/article/pii/0021979779902868>.
- Goldstein, H., 1980. *Classical Mechanics*, second ed.
- Haider, A., Levenspiel, O., 1989. Drag coefficient and terminal velocity of spherical and nonspherical particles. *Powder Technol.* 58 (1), 63–70. [http://dx.doi.org/10.1016/0032-5910\(89\)80008-7](http://dx.doi.org/10.1016/0032-5910(89)80008-7), URL <https://www.sciencedirect.com/science/article/pii/0032591089800087>.
- Happel, J., Brenner, H., 1983. *Low Reynolds Number Hydrodynamics*. Martinus Nijhoff Publishers, Kluwer, The Hague, Netherlands.
- Högberg, S.M., Åkerstedt, H.O., Lundström, S., Freund, J.B., 2008. Numerical model for fiber transport in the respiratory airways.
- Hölzer, A., Sommerfeld, M., 2008. New simple correlation formula for the drag coefficient of non-spherical particles. *Powder Technol.* 184 (3), 361–365. <http://dx.doi.org/10.1016/j.powtec.2007.08.021>.
- Inthavong, K., Shang, Y., Del Gaudio, J.M., Wise, S.K., Edwards, T.S., Bradshaw, K., Wong, E., Smith, M., Singh, N., 2021. Inhalation and deposition of spherical and pollen particles after middle turbinate resection in a human nasal cavity. *Respir. Physiol. Neurobiol.* 294, 103769. <http://dx.doi.org/10.1016/j.resp.2021.103769>, URL <https://www.sciencedirect.com/science/article/pii/S1569904821001543>.
- Jain, R., Tschigale, S., Fröhlich, J., 2021. Impact of shape: DNS of sediment transport with non-spherical particles. *J. Fluid Mech.* 916, A38. <http://dx.doi.org/10.1017/jfm.2021.214>.
- Jaklič, A., Leonardis, A., Solina, F., 2000. Superquadrics and Their Geometric Properties, Vol. 20. pp. 13–39. http://dx.doi.org/10.1007/978-94-015-9456-1_2.
- Jeffery, G., 1922. The motion of ellipsoidal particles immersed in a viscous fluid. *Proc. R. Soc. London. Ser. A, Containing Pap. A Math. Phys. Character.* 102 (715), 161–179. <http://dx.doi.org/10.1098/rspa.1922.0078>, URL <https://royalsocietypublishing.org/>.

- Koseff, J.R., Street, R.L., 1984. The lid-driven cavity flow: A synthesis of qualitative and quantitative observations. *J. Fluids Eng.* 106 (4), 390–398. <http://dx.doi.org/10.1115/1.3243136>, arXiv:https://asmedigitalcollection.asme.org/fluidsengineering/article-pdf/106/4/390/5513579/390_1.pdf.
- Koullapis, P.G., Kassinos, S.C., Bivolarova, M.P., Melikov, A.K., 2016. Particle deposition in a realistic geometry of the human conducting airways: Effects of inlet velocity profile, inhalation flowrate and electrostatic charge. *J. Biomech.* 49 (11), 2201–2212. <http://dx.doi.org/10.1016/j.jbiomech.2015.11.029>.
- Koullapis, P., Kassinos, S.C., Muela, J., Perez-segarrá, C., Rigola, J., Lehmkuhl, O., Cui, Y., Sommerfeld, M., Elcner, J., Jicha, M., Saveljic, I., Filipovic, N., Lizal, F., Nicolaou, L., 2017. Regional aerosol deposition in the human airways: The SimInhale benchmark case and a critical assessment of in silico methods. *Eur. J. Pharm. Sci.* 113, 1–18. <http://dx.doi.org/10.1016/j.ejps.2017.09.003>.
- Lamb, H., 1994. *Handbook of Fluid Dynamics*, sixth ed. Cambridge University Press.
- Leith, D., 1987. Drag on nonspherical objects. *Aerosol Sci. Technol.* 6 (2), 153–161. <http://dx.doi.org/10.1080/02786828708959128>.
- Lizal, F., Cabalka, M., Maly, M., Elcner, J., Belka, M., Sujanska, E.L., Farkas, A., Starha, P., Pech, O., Misik, O., Jedelsky, J., Jicha, M., 2022. On the behavior of inhaled fibers in a replica of the first airway bifurcation under steady flow conditions. *Aerosol Sci. Technol.* 56 (4), 367–381. <http://dx.doi.org/10.1080/02786826.2022.2027334>.
- Marijnissen, J., Zeckendorf, A., Lemkowitz, S., Bibo, H., 1991. Transport and deposition of uniform respirable fibres in a physical lung model. *J. Aerosol Sci.* 22 (1), 859–862.
- Maxey, M.R., Riley, J.J., 1983. Equation of motion for a small rigid sphere in a nonuniform flow. *Phys. Fluids* 26 (4), 883–889. <http://dx.doi.org/10.1063/1.864230>, URL <https://aip.scitation.org/doi/abs/10.1063/1.864230>.
- Michel, A., Arcen, B., 2021. Reynolds number effect on the concentration and preferential orientation of inertial ellipsoids. *Phys. Rev. Fluids* 6, <http://dx.doi.org/10.1103/PhysRevFluids.6.114305>.
- Myojo, T., 1987. Deposition of fibrous aerosol in model bifurcating tubes. *J. Aerosol Sci.* 18 (3), 337–347. [http://dx.doi.org/10.1016/0021-8502\(87\)90027-9](http://dx.doi.org/10.1016/0021-8502(87)90027-9), URL <https://www.sciencedirect.com/science/article/pii/0021850287900279>.
- Myojo, T., 1990. The effect of length and diameter on the deposition of fibrous aerosol in a model lung bifurcation. *J. Aerosol Sci.* 21 (5), 651–659. [http://dx.doi.org/10.1016/0021-8502\(90\)90120-M](http://dx.doi.org/10.1016/0021-8502(90)90120-M), URL <https://www.sciencedirect.com/science/article/pii/002185029090120M>.
- Myojo, T., Takaya, M., 2001. Estimation of fibrous aerosol deposition in upper bronchi based on experimental data with model bifurcation. *Ind. Health* 39(2), 141–149.
- Okabe, K., Murthy, G.G.K., Vallarino, J.A., Skornik, W.A., Hatch, V.C., Kater, M.R., Tsuda, A., Godleski, J.J., 1997. Deposition efficiency of inhaled fibers in the hamster lung. *Inhal. Toxicol.* 9 (2), 85–98. <http://dx.doi.org/10.1080/089583797198286>.
- OpenFOAM The OpenFOAM Foundation, 2020. OpenFOAM foundation repository for OpenFOAM version 7. URL <https://github.com/OpenFOAM/OpenFOAM-7>. (Accessed 18 November 2020).
- Ravnik, J., Štrakl, M., Wedel, J., Steinmann, P., Hriberšek, M., 2022. Stokes flow induced drag and torque on asbestos-like fibres can not be estimated by a simplistic ellipsoidal approximation. In: 45th International Conference on Boundary Elements and Other Mesh Reduction Methods Organized By WIT - Wessex Institute of Technology, U.K..
- Saccone, D., Marchioli, C., De Marchis, M., 2022. Effect of roughness on elongated particles in turbulent channel flow. *Int. J. Multiph. Flow.* 152, 104065. <http://dx.doi.org/10.1016/j.ijmultiphaseflow.2022.104065>, URL <https://www.sciencedirect.com/science/article/pii/S0301932222000751>.
- Sanjeevi, S.K., Kuipers, J., Padding, J.T., 2018. Drag, lift and torque correlations for non-spherical particles from Stokes limit to high Reynolds numbers. *Int. J. Multiph. Flow.* 106, 325–337. <http://dx.doi.org/10.1016/j.ijmultiphaseflow.2018.05.011>, URL <https://www.sciencedirect.com/science/article/pii/S0301932217307851>.
- Shankar, P.N., Deshpande, M.D., 2000. Fluid mechanics in the driven cavity. *Annu. Rev. Fluid Mech.* 32 (1), 93–136. <http://dx.doi.org/10.1146/annurev.fluid.32.1.93>.
- Štrakl, M., Hriberšek, M., Wedel, J., Steinmann, P., Ravnik, J., 2022a. A model for translation and rotation resistance tensors for superellipsoidal particles in Stokes flow. *J. Mar. Sci. Eng.* 10 (3), 369.
- Štrakl, M., Wedel, J., Hriberšek, M., Steinmann, P., Ravnik, J., 2022b. Tensor coefficient model for superellipsoids. URL <https://github.com/transport-phenomena/superellipsoid-force-torque-model>. (Accessed 02 March 2022).
- Su, W.-C., Cheng, Y., 2006. Fiber deposition pattern in two human respiratory tract replicas. *Inhal. Toxicol.* 18, 749–760. <http://dx.doi.org/10.1080/08958370600748513>.
- Tian, L., Ahmadi, G., 2013. Fiber transport and deposition in human upper tracheo-bronchial airways. *J. Aerosol Sci.* 60, 1–20. <http://dx.doi.org/10.1016/j.jaerosci.2013.02.001>.
- Tian, L., Ahmadi, G., Wang, Z., Hopke, P.K., 2012. Transport and deposition of ellipsoidal fibers in low Reynolds number flows. *J. Aerosol Sci.* 45, 1–18. <http://dx.doi.org/10.1016/j.jaerosci.2011.09.001>, URL <https://www.sciencedirect.com/science/article/pii/S0021850211001571>.
- Tsornig, S., Capart, H., Lo, D., Lai, J.-S., Young, D.-L., 2008. Behaviour of macroscopic rigid spheres in lid-driven cavity flow. *Int. J. Multiph. Flow.* 34, 76–101. <http://dx.doi.org/10.1016/j.ijmultiphaseflow.2007.06.007>.
- Voth, G., Soldati, A., 2017. Anisotropic particles in turbulence. *Annu. Rev. Fluid Mech.* 49, 249–276. <http://dx.doi.org/10.1146/annurev-fluid-010816-060135>.
- Wang, Y., Zhou, L., Wu, Y., Yang, Q., 2018. New simple correlation formula for the drag coefficient of calcareous sand particles of highly irregular shape. *Powder Technol.* 326, 379–392.
- Wedel, J., Steinmann, P., Štrakl, M., Hriberšek, M., Cui, Y., Ravnik, J., 2022. Anatomy matters: the role of the subject-specific respiratory tract on aerosol deposition – a CFD study. *Comput. Methods in Appl. Mech. Eng.* 401, 115372. <http://dx.doi.org/10.1016/j.cma.2022.115372>.
- Wedel, J., Steinmann, P., Štrakl, M., Hriberšek, M., Ravnik, J., 2021a. Can CFD establish a connection to a milder COVID-19 disease in younger people? *Comput. Mech.* 67, 1497–1513. <http://dx.doi.org/10.1007/s00466-021-01988-5>.
- Wedel, J., Steinmann, P., Štrakl, M., Hriberšek, M., Ravnik, J., 2021b. Risk assessment of infection by airborne droplets and aerosols at different levels of cardiovascular activity. *Arch. Comput. Methods Eng.* 28, 4297–4316. <http://dx.doi.org/10.1007/s11831-021-09613-7>.
- Weibel, E.R., 1963. *Morphometry of the Human Lung*. Academic Press, New York.
- Weller, H.G., Tabor, G., Jasak, H., Fureby, C., 1998. A tensorial approach to computational continuum mechanics using object orientated techniques. *Comput. Phys.* 12, 620–631. <http://dx.doi.org/10.1063/1.168744>.
- Wellmann, C., Lillie, C., Wriggers, P., 2008. A contact detection algorithm for superellipsoids based on the common-normal concept. *Eng. Comput.* 25, <http://dx.doi.org/10.1108/02644400810881374>.
- Wu, K., Sun, W., Liu, S., Cai, G., 2021. Influence of particle shape on the shear behavior of superellipsoids by discrete element method in 3D. *Adv. Powder Technol.* 32 (11), 4017–4029.
- You, Y., Zhao, Y., 2018. Discrete element modelling of ellipsoidal particles using super-ellipsoids and multi-spheres: A comparative study. *Powder Technol.* 331, 179–191. <http://dx.doi.org/10.1016/j.powtec.2018.03.017>, URL <https://www.sciencedirect.com/science/article/pii/S0032591018302080>.
- Zastawny, M., Mallouppas, G., Zhao, F., van Wachem, B., 2012. Derivation of drag and lift force and torque coefficients for non-spherical particles in flows. *Int. J. Multiph. Flow.* 39, 227–239. <http://dx.doi.org/10.1016/j.ijmultiphaseflow.2011.09.004>, URL <https://www.sciencedirect.com/science/article/pii/S0301932211002047>.
- Zhang, H., Ahmadi, G., Fan, F.-G., McLaughlin, J.B., 2001. Ellipsoidal particles transport and deposition in turbulent channel flows. *Int. J. Multiph. Flow.* 27 (6), 971–1009. [http://dx.doi.org/10.1016/S0301-9322\(00\)00064-1](http://dx.doi.org/10.1016/S0301-9322(00)00064-1), URL <https://www.sciencedirect.com/science/article/pii/S0301932200000641>.
- Zhang, L., Asgharian, B., Anjilvel, S., 1996. Inertial and interceptional deposition of fibers in a bifurcating airway. *J. Aerosol Med.* 9 (3).
- Zhang, H., Li, D., Xie, L., Xiao, Y., 2015. Documentary research of human respiratory droplet characteristics. In: *Procedia Engineering* (Ed.), 9th International Symposium on Heating, Ventilation and Air Conditioning (ISHVAC) and the 3rd International Conference on Building Energy and Environment (COBEE), Vol. 121. pp. 1365–1374.
- Zhang, B., Xu, D., Bingchang, Z., Ji, C., Munjiza, A., Williams, J., 2020. Numerical investigation on the incipient motion of non-spherical sediment particles in bedload regime of open channel flows. *Comput. Part. Mech.* 7, <http://dx.doi.org/10.1007/s40571-020-00323-8>.